# Photocontrol of endogenous glycine receptors *in vivo*

Alexandre M.J. Gomila[1], Karin Rustler[2], Galyna Maleeva[1,3], Alba Nin-Hill[4], Daniel Wutz[2], Antoni Bautista-Barrufet[1], Xavier Rovira[1,12], Miquel Bosch[1,13], Elvira Mukhametova[3,5], Elena Petukhova[6], Daria Ponomareva[6], Marat Mukhamedyarov[6], Franck Peiretti[7], Mercedes Alfonso-Prieto[8,9], Carme Rovira[4,10*], Burkhard König[2*], Piotr Bregestovski[3,6*], Pau Gorostiza[1,10,11,14*]

1. Institute for Bioengineering of Catalonia (IBEC), The Barcelona Institute of Science and Technology (BIST), Barcelona 08028, Spain
2. University of Regensburg, Institute of Organic Chemistry, Regensburg 93053, Germany
3. Aix-Marseille Université, INSERM, INS, Institut de Neurosciences des Systèmes, Marseille 13005, France
4. University of Barcelona, Department of Inorganic and Organic Chemistry, Institute of Theoretical Chemistry (IQTCUB), Barcelona 08028, Spain
5. Kazan Federal University, Open Lab of Motor Neurorehabilitation, Kazan, Russia
6. Institute of Neurosciences, Kazan State Medical University, Kazan, Russia
7. Aix Marseille Université, INSERM 1263, INRA 1260, C2VN, Marseille, France
8. Institute for Advanced Simulation IAS-5 and Institute of Neuroscience and Medicine INM-9, Computational Biomedicine, Forschungszentrum Jülich, 52425 Jülich, Germany
9. Cécile and Oskar Vogt Institute for Brain Research, Medical Faculty, Heinrich Heine University Düsseldorf, 40225 Düsseldorf, Germany
10. Catalan Institution for Research and Advanced Studies (ICREA), Barcelona 08003 Spain
11. CIBER-BBN, Madrid 28001 Spain
12. Present address: Molecular Photopharmacology Research Group, The Tissue Repair and Regeneration Laboratory, University of Vic–Central University of Catalonia, Carrer de la Laura, 13, 08500 Vic, Spain
13. Present address: Institut d'Investigacions Biomèdiques August Pi i Sunyer, Barcelona, Spain
14. Lead Contact

*Corresponding authors: c.rovira@ub.edu (C. R.), burkhard.koenig@chemie.uni-regensburg.de (B. K.), pbreges@gmail.com (P. B.), pau@icrea.cat (P.G.)

## Highlights

• The photochromic small molecule Glyght enables control of glycine receptors with light

• Glyght is active and selective in endogenous human and zebrafish receptors

• Glyght is reversible in endogenous human and zebrafish receptors *in vitro* and *in vivo*

• Glyght constitutes a new molecular scaffold for glycine receptor pharmacology

## Summary

Glycine receptors (GlyRs) are indispensable for maintaining excitatory/inhibitory balance in neuronal circuits that control reflexes and rhythmic motor behaviors. Here we have developed Glyght, a GlyR ligand controlled with light. It is selective over other Cys-loop receptors, is active in vivo, and displays an allosteric mechanism of action. The photomanipulation of glycinergic neurotransmission opens new avenues to understanding inhibitory circuits in intact animals and to developing drug-based phototherapies.

## Keywords

glycine receptors, in vivo, photopharmacology, optopharmacology, inhibitory, neurotransmission, CNS, photoswitch

## Main Text

The control of biological activity with light has become a powerful tool for understanding complex multicellular (Guglielmi et al., 2015) and intracellular processes (Shin et al., 2018) and protein dynamics (Lichtenegger et al., 2018; Reiner and Isacoff, 2014), as well as for developing novel therapeutic strategies (Lichtenegger et al., 2018). In particular, optogenetics (Rost et al., 2017) and photopharmacology (Hüll et al., 2018) have been a boon to neurobiology, empowering it to control neuronal receptor activity with subtype pharmacological selectivity and micrometric resolution (Pittolo et al., 2014, 2019), fire individual neurons (Shemesh et al., 2017), and map their connectivity and strength (Izquierdo-Serra et al., 2018).

Photoswitchable ligands (Hüll et al., 2018) enable directly controlling the activity of endogenous receptors without requiring genetic manipulation (Izquierdo-Serra et al., 2016; Pittolo et al., 2014). They can be applied to intact tissue, making drug-based phototherapies possible. Despite the importance of inhibitory receptors, few photoswitches targeting ionotropic gamma amino butyric acid receptors ($GABA_A$Rs) have been reported (Huckvale et al., 2016; Maleeva et al., 2019; Stein et al., 2012; Yue et al., 2012), and no specific modulator has been developed for glycine receptors (GlyRs).

GlyRs and $GABA_A$Rs belong to the pentameric Cys-loop superfamily along with excitatory nicotinic acetylcholine receptors (nAChRs) and serotonin receptors (5-$HT_3$Rs). $GABA_A$Rs and GlyRs share not only the pentameric assembly of their subunits and the inhibitory regulation of cell membrane potential through their chloride-selective pore, but also the mechanism of agonist-induced desensitization, which is driven by homologous residues between transmembrane domains (TMDs) of the receptor (Gielen et al., 2015). These similarities hamper the development of selective ligands.

Alterations in inhibitory neurotransmission cause an excitation/inhibition disbalance that has been linked to many and etiologically diverse neurological diseases, from epilepsy to anxiety, autism (Berry-Kravis et al., 2017), and schizophrenia (Rudolph et al., 2001). Modulating neuronal inhibition with systemically administered drugs can partially restore balance and reduce certain symptoms, but the efficacy of these strategies is very limited in diseases where specific circuits are altered. In these cases, what matters is the precise location and timing of inhibition to restore homeostasis, and cure is unlikely even with the most pharmacologically selective drugs.

In particular, glycinergic transmission regulates the majority of reflex and rhythmic motor behaviors, including locomotion and breathing (Schmid et al., 1996). Normal functioning of locomotor circuits relies on a strictly determined equilibrium between excitatory and inhibitory synapses onto interneurons (Li and Moult, 2012). Disruptions to this balance trigger locomotor dysfunctions (Hirata et al., 2005). Insufficient GlyR function leads to excessive startle response (hyperekplexia) and other pathologies (Hennermann et al., 2012; Schaefer et al., 2017). Despite the importance of glycinergic neurotransmission, the

repertoire of GlyR drugs available is still extremely limited (Burgos et al., 2016; Yevenes and Zeilhofer, 2011) and not highly specific (Lynch et al., 2017). Strychnine and tropisetron remain the only modulators that show selectivity for GlyR over $GABA_AR$, but the former is also an nAChR antagonist (Jensen et al., 2006; Kuijpers et al., 1994), and the latter antagonizes 5-$HT_3R$ (Chesnoy-Marchais, 1996; Yang et al., 2007). Selective GlyR drugs are necessary to treat hyperekplexia, autism, chronic inflammatory pain, breathing disorders, temporal lobe epilepsy, alcoholism, and motor neuron disease (Lynch et al., 2017). However, given the diversity and ubiquity of glycinergic circuits, traditional pharmacology is unlikely to be enough unless the activity of these ligands can be modulated right at the specific circuits involved in every disease.

Here, we initially aimed at developing photoswitchable ligands of $GABA_ARs$ based on benzodiazepines. Azo-compounds (3a-d, Figure 1A) were thus designed to display *cis-trans* photochromism while maintaining the ability of the nitrazepam moiety to bind the $GABA_AR$, as reported for other substitutions at the same position of the ligand (Menezes et al., 2012). Unexpectedly, we obtained a GlyR-selective negative allosteric modulator whose inhibitory action at GlyRs was increased under UV light (*cis*-on) and which we named Glyght (short for "GlyR controlled by light").

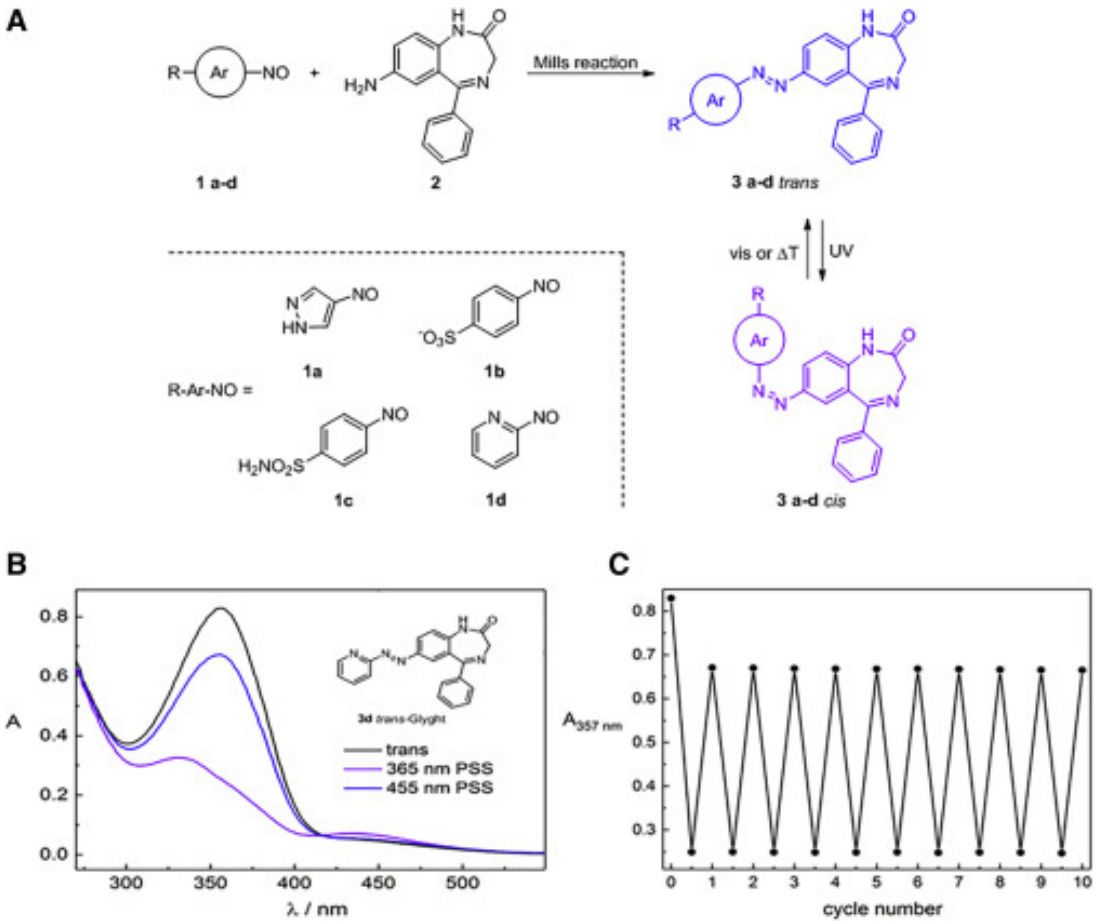


**Figure 1. Synthetic Strategy of Photochromic Derivatives of Benzodiazepine**
(A) General scheme for synthesizing azobenzene derivatives of benzodiazepine with different substitutions via the Mills reaction (3a–d). The resulting *trans-cis* photoisomerization is indicated. (B) UV/VIS absorption spectrum showing the photochromic behavior of compound 3d (Glyght, 50 µM in DMSO) from the *trans* isomer (black trace) at its thermal equilibrium, the photostationary

state (PSS) under illumination with 365 nm (purple), and the PSS under illumination with 455 nm (blue).
(C) Cycle performance of 3d (Glyght, 50 μM in DMSO). Changes in absorption at 357 nm were measured during alternate illumination with light of 365 nm for 15 s and 455 nm for 3 s.

The photochromic azo moiety was introduced via a Mills reaction of several nitroso aryl moieties (compounds 1a–d, Figure 1A) with the amino-substituted benzene in the structure of 7-aminonitrazepam (7AN; compound 2, Figure 1A, obtained as reported; Guandalini et al., 2008; Severino et al., 2008). All derivatives reversibly photoswitch at 365 nm (*trans* to *cis* isomerization) and 455 to 530 nm (*cis* to *trans* isomerization), as exemplarily shown for the pyridine-based derivative 3d (Glyght) (Figures 1B and 1C). Thermal relaxation half-lives in the dark are longer than 1 h (Table S1).

To characterize the photopharmacological effects of compounds 3a–d, we designed a behavioral assay to record and quantify the swimming activity of zebrafish larvae as a function of illumination. Zebrafish express all $GABA_AR$ and GlyR subunits, with high sequence similarity to the mammalian receptors (Imboden et al., 2001), and larvae display full exploratory capacities at 7 days post fertilization (dpf) (Kimmel et al., 1995; Liu et al., 2015; MacPhail et al., 2009). Ligands of inhibitory receptors should alter the well-known behavioral activity of the larvae and be correlated to specific dynamic traits such as swimming-speed variations, transition swimming patterns, or anxiety-like behaviors (Lee et al., 2012; Schnörr et al., 2012). In order to identify alterations in inhibitory neurotransmission, we focused on fast movements and measured swimming distances and duration of high-speed swimming (Bencan et al., 2009; Cui et al., 2005; Hirata et al., 2005; Lee et al., 2012). Individual larvae were placed in separate wells of a 96 well plate (Figure 2A), each containing different solution conditions, including nonphotoswitchable control drugs like the $GABA_AR$ potentiator 7AN (2), the photochromic compounds 3a–d at different concentrations, and vehicle (1% DMSO). The setup (see STAR Methods for details) allows maintaining the animals in the dark and subjecting them to cycles of illumination at 365 and 455 nm. The inset of Figure 2A shows exemplary 1 min trajectories of individual fish in wells containing vehicle and compound 3d (Glyght, 100 μM) during the resting period (RP), under 365 nm light (UV), and under 455 nm light (visible, VIS). Green and red trajectories plot slow and fast swimming periods, respectively. Videos of the entire plate during the RP and photoswitching experiment can be viewed in Video S1. The time course (integrated every minute for 12 animals) is shown in Figure 2B. During the RP, Glyght-treated animals display enhanced locomotion compared with controls. Although control animals are startled by UV light and slowed down by VIS light, the increase in locomotion displayed by treated animals is significantly higher (Figure S1E) and is maintained over long periods of time (Figure S1D). The results of all photoswitches (3a–d), 7AN (2), and vehicle are shown in Figure 2C. In all cases, the time spent in fast swimming (see STAR Methods for details) is longer under UV than under VIS light, but only for Glyght (3d) is this difference higher than for controls. In order to identify photoswitchable hits, we assumed larval swimming activity as the quantifiable variable, and we defined light periods as intrinsically dependent variables of larva behavioral outcomes. We calculated the ratio between the activities under UV and under VIS light (UV/VIS activity ratio, UVAR) and used it as a score to identify compounds producing photoswitchable behaviors. Three compounds displayed UVARs significantly different from those of the control (UVAR of endogenous photo responses in vehicle, Figure S1A). One was excluded due to precipitation over time (3c) and two were retained for further studies: 3b (azo-NZ1, a $GABA_AR$ blocker reported in a separate article; Maleeva et al., 2019), and 3d (Glyght), characterized below. For Glyght, we confirmed the hit in 5 independent experiments from

different larvae batches (Figures S1B and S1C) and verified that photo responses are dose dependent (Figure 2D) before moving on to in vitro pharmacological characterizations with an activity assay.

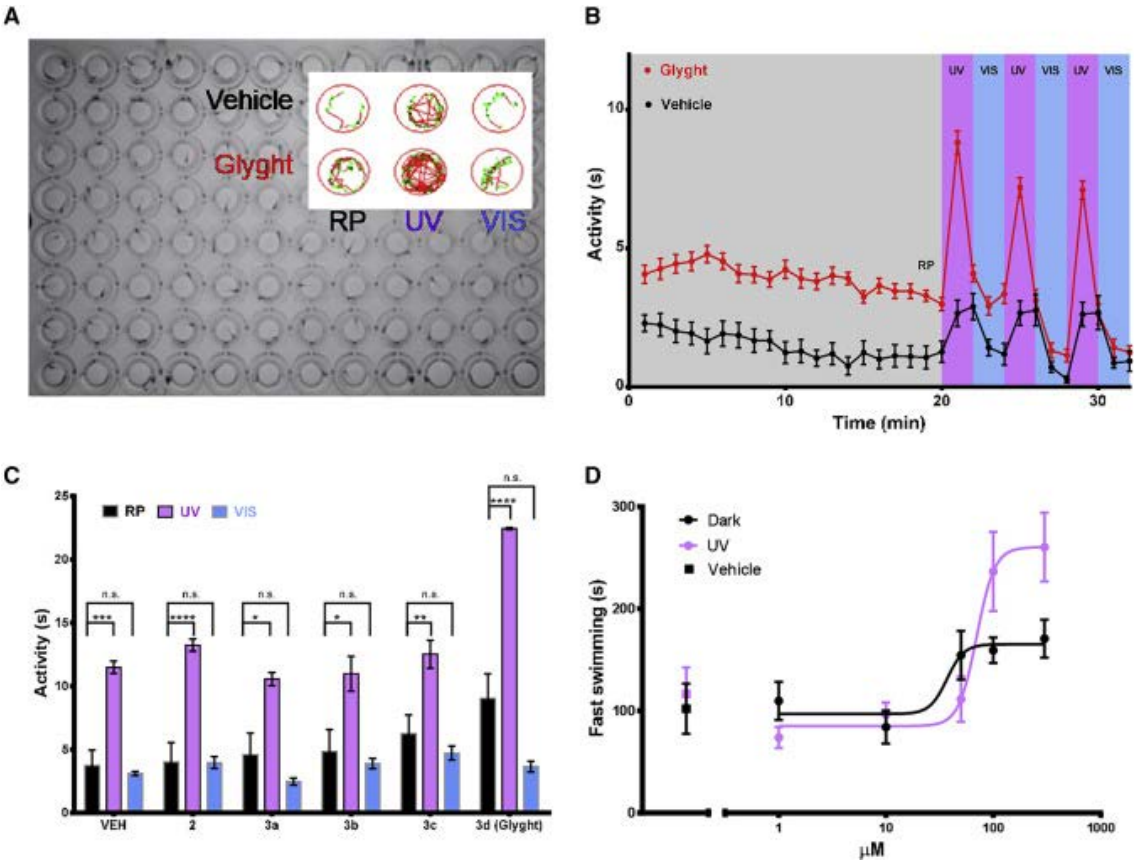


**Figure 2. *In Vivo* Identification of Behavioral Outcomes for Photoswitchable Derivatives**
(A) A 96 well plate with individual zebrafish larvae in each well exposed to different solutions and conditions. Video recordings of the entire plate under different illumination conditions (dark, 365 nm, 455 nm) allow analyzing the motility of individual animals in order to identify drug- and light-dependent activities. Inset: Detail of two wells containing vehicle (1% DMSO, top) and compound 3d (Glyght, bottom) and the trajectories swum by individual larvae during the resting, UV, and visible periods (RP, UV, VIS, respectively). Different swimming velocities during each trajectory are automatically categorized by the software and are indicated in green (2–6 mm·s$^{-1}$) and red (faster than 6 mm·s$^{-1}$).

(B) Fast swimming (FS; time spent swimming faster than 6 mm·s$^{-1}$) of individual larvae exposed to vehicle and Glyght during RP, UV, and VIS illumination was integrated into 1 min data points. Error bars indicate the SEM of FS in each 1 min period for 12 individual larvae.

(C) Quantification of larvae activity (n = 8) during RP (averaged over 2 min) and during UV and VIS periods (averaged over 3 cycles) in 7-aminonitrazepam ((2), nonphotoswitchable GABAAR modulator), vehicle, and a panel of four photochromic ligands (3a–d). Glyght displays significantly higher activity during RP and UV periods, suggesting basal and UV-enhanced antagonism of inhibitory receptors. ∗p ≤ 0.05, ∗∗p ≤ 0.01, ∗∗∗p ≤ 0.001, ∗∗∗∗p ≤ 0.0001. Error bars represent SEM.

(D) Dose response for Glyght in FS (in seconds) according to the last 2 min of RP (Dark trace) and 2 min of 365 nm illumination (UV trace). Dark trace activity corresponds to pure *trans*-Glyght and UV trace to isomerized *cis*-Glyght. Error bars represent SEM for n = 8 larvae per concentration group and traces fitted with sigmoidal four-parameters model.

**Video S1. In Vivo Photoswitchable Assay, Related to Figure 2: [https://www.cell.com/cell-chemical-biology/fulltext/S2451-9456(20)30302-0](https://www.cell.com/cell-chemical-biology/fulltext/S2451-9456(20)30302-0)**

*Danio rerio* 7 dpf larvae are individually placed in a 96 well plate and tracked using infrared video recording.

Four treatment groups are labeled as Water (Control group), VEH (vehicle), 7AN (7-aminonitrazepam), and Glyght (compound 3d).

Light transitions are labeled as UV (365 nm) and VIS (455 nm).

We used electrophysiological recordings to measure agonist-induced responses in anion-selective $GABA_AR$s and GlyRs and in cation-selective 5-$HT_3$Rs and AChRs at heterologous expression (see STAR Methods for details) and evaluated the effects of adding Glyght. The results are shown in Figures 3A–3C and Figures S2 and S3. In contrast to the effect of diazepam on $GABA_AR$s (Griffin et al., 2013), Glyght displayed a weak action on α1/β2/γ2 $GABA_AR$s: in the presence of 50 μM *trans*-Glyght, 5 μM GABA-induced currents were inhibited by only 9% ± 2% (n = 6) and 300 μM GABA currents by 14% ± 4% (n = 5) (Figure S2A). UV light prevented the weak current inhibition of $GABA_AR$ by Glyght.

Since the action of Glyght on $GABA_AR$s cannot account for the robust behavioral effects observed in fish (Figure 2), we asked whether this compound might interact with other inhibitory ligand-gated receptors responsible for the control of movement (Lynch et al., 2017; Ogino and Hirata, 2016), namely GlyR. Thus, we tested Glyght in zebrafish $\alpha_1$ ($\alpha_{1Z}$) and $\alpha_2$ ($\alpha_{2Z}$) homomeric GlyRs during activation by a nonsaturating concentration of glycine (see STAR Methods). In $\alpha_{1Z}$ GlyRs, *trans*-Glyght (50 μM) reduced the current amplitude by 33% ± 4% (Figure S2B), and stronger reduction was observed upon isomerizing it to *cis*-Glyght under 365 nm light (53% ± 5%, n = 8). Receptor photoswitching was stronger on $\alpha_{2Z}$ GlyRs, wherein 50 μM *trans*-Glyght and *cis*-Glyght reduced glycine currents by 32% ± 3% and 74% ± 5%, respectively (Figure 3C and S2E–S2G, n = 7). When Glyght was coapplied with saturating concentrations of glycine, its effect become negligible, clearly indicating that the compound is not an open-channel blocker (Figures S2C and S2D, n = 3; S2F–S2G, n = 3). Full dose-response curves under UV and dark conditions in these receptors confirmed that $\alpha_{2Z}$ GlyRs are more sensitive to Glyght than $\alpha_{1Z}$ GlyRs (Figure S2I and S2J). Importantly, these results were confirmed in mammalian GlyRs, where Glyght caused strong *cis*-on inhibition in all homomeric and heteromeric receptors ($\alpha_1$, $\alpha_2$, $\alpha_{1\beta}$, and $\alpha_{2\beta}$; Figures 3A, 3B, S3A, S3B, S3D, and S3E). No illumination-dependent outcome was observed using other inhibitors like picrotoxin (Figures S3C and S3F).

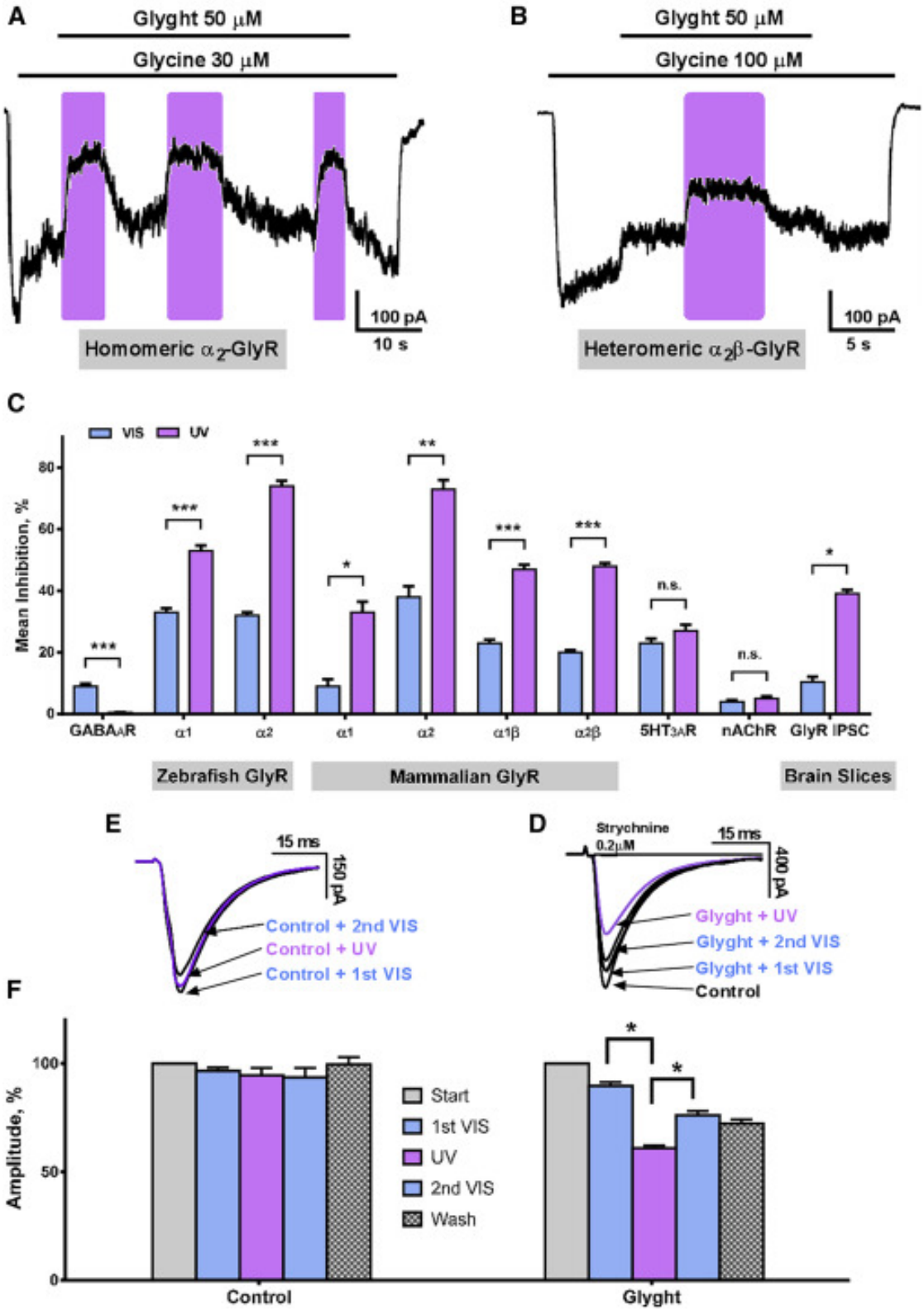


**Figure 3. Glyght Is a GlyR-Selective Photoswitch**

(A) Representative trace illustrating the photoswitchable effect of Glyght (50 μM) on currents mediated by GlyR composed of α2 subunits. Note an increase in the inhibitory efficiency of Glyght upon illumination with UV light. The duration of glycine and Glyght application is indicated by black bars above traces; the duration of UV illumination is indicated by violet rectangles (Vhold = −30 mV).

(B) Representative trace illustrating the photoswitching action of Glyght (50 μM) on currents mediated by heteromeric α2/β GlyRs (Vhold = −30 mV).

(C) Cumulative graph demonstrating the percentage of Glyght (50 μM)-induced inhibition under visible (blue) and UV (violet) light on different types of Cys-loop receptors. ∗p ≤ 0.05, ∗∗p ≤ 0.01, ∗∗∗p ≤ 0.001.

(D) Superimposed average traces of glycinergic inhibitory postsynaptic currents (IPSCs) recorded at perfusion of the slices with Glyght-free solution under illumination by blue and UV light, as indicated. Note the absence of the influence of different wavelengths of light on the amplitude of eIPSCs. Strychnine (0.2 μM) completely abolished eIPSCs, confirming their glycinergic nature. Example from the P4 mouse.

(E) Superimposed traces of average eIPSCs recorded in Glyght-free solution (Control) and after addition of 100 μM Glyght at illumination with blue or UV light, as indicated. Brain-stem slice from the P5 mouse. Note strong inhibition of the current amplitude under UV (*cis*-Glyght) and its restoration under blue (*trans*-Glyght) illumination.

(F) Summary of results from 5 motoneurons obtained at recording in Glyght-free solution (Control) and 7 motoneurons in the presence of 100 μM Glyght under illumination with blue or UV light. Columns represent the amplitudes of IPSCs normalized with respect to control. ∗Significant difference with $p < 0.05$ (paired-sample Wilcoxon signed rank test).

Since Glyght displays selectivity for GlyRs compared with GABAARs (Figure 3C), we further characterized its activity in other pentameric receptors. The compound displayed low activity and no photoswitching in 5-HT3ARs (Figures 3C, S3G, and S3H) and was completely inactive in muscular nAChRs (Figure S3I).

Finally, using whole-cell patch clamp recordings, we performed analysis of Glyght action on the amplitude of the evoked glycinergic inhibitory postsynaptic currents (eIPSCs) in hypoglossal motoneurons of brain-stem slices (Petukhova et al., 2018) (see STAR Methods for details). At holding potential (Vhold) −70 mV, the mean amplitude of eIPSCs varied in different cells in the range 30–700 pA. In the absence of the photochrome the synaptic currents were not perturbed by blue or UV light (n = 5; Figures 3D and 3E). Addition of Glyght at a concentration of 100 μM under illumination with blue light (photochrome in *trans* configuration) it slightly affected the amplitude of the glycinergic eIPSCs. On average, following 5–10 min of Glyght application, the amplitude of eIPSCs decreased to 89.6% ± 4.5% (n = 7; Figures 3D and 3F). Illumination of Glyght by UV (transition to *cis* state) resulted in the decrease of mean eIPSC amplitude to 60.9% ± 3.3% ($p < 0.05$). Subsequent illumination of Glyght-containing solution by blue light restored the amplitude to 76% ± 5.5% ($p < 0.05$). During washing, the amplitude of the glycinergic eIPSCs under Glyght-free conditions did not change relative to the previous incubation in a solution containing Glyght illuminated by blue light: it was 72.3% ± 4.8% (n = 7; Figures 3E and 3F). This continuous decrease in the mean eIPSC resulted in the small continuous rundown during the whole-cell recordings. The glycinergic nature of eIPSCs was confirmed by their complete abolition under the action of strychnine at a concentration of 0.2 μM (Figure 3E). These observations confirm the light-controllable modulation of glycinergic inhibitory postsynaptic currents by Glyght in the hypoglossal motoneurons of brain-stem slices.

All these results are summarized in Figure 3C and indicate that Glyght is broadly active in homo- and heteromeric GlyRs from fish and mammals and remarkably selective versus all other members of the Cys-loop receptor family.

To understand the photopharmacological profile of Glyght we turned to modeling of the compound in the open (agonist-bound) structure of $\alpha_{1Z}$ GlyR (Du et al., 2015). Molecular dockings showed that neither of the Glyght isomers can bind at the channel pore (in

agreement with our patch-clamp results), that *trans*-Glyght displays moderate binding in several regions of the extracellular domain (ECD) and the TMD, and that *cis*-Glyght poses to a non-glycine site at the ECD/TMD interface (displayed in blue and violet, respectively, Figure 4 and S4). We focused on the latter binding site, since it is the region showing the largest differences in ligand pose densities for both $\alpha_{1Z}$ and $\alpha_{2H}$ GlyRs. Moreover, this site includes key residues for channel activation and conductance (Du et al., 2015; Lynch et al., 1997; Ryan et al., 1994) and is involved in allosteric coupling between ligand binding to the ECD and ion channel pore opening in the TMD (Andersen et al., 2011; Bertozzi et al., 2016; Cederholm et al., 2009; Jaiteh et al., 2016; Wulff et al., 2009). As shown in Figure 4H, *cis*-Glyght binds farther inside the ECD/TMD interface than *trans*-Glyght, in line with its stronger effect. Moreover, *trans*-Glyght can mediate the interaction between M2-M3 and β1-β2 loops that stabilizes the open channel state (Du et al., 2015) (blue arrow in Figure 4H). On the other hand, *cis*-Glyght favors the interaction between M2-M3 and β8-β9 loops, which are associated with the closed state (purple arrow in Figure 4H). These results are in full agreement with the stronger inhibition of GlyRs observed for *cis*-Glyght in Figure 3.

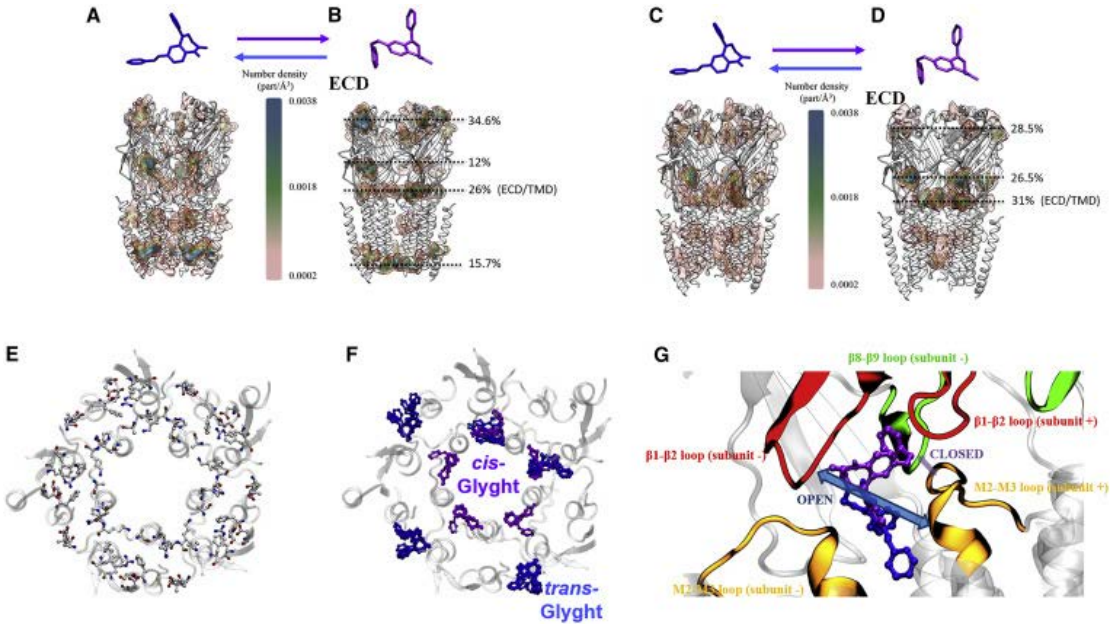


**Figure 4. Computational Approach for Glyght Selectivity**

(A) Density map of the ligand poses of *trans*-Glyght (conformers M and P) obtained in the blind docking with the $\alpha_{1Z}$GlyR cryo-EM structure (Du et al., 2015), which represents an open state. Each contour line corresponds to a number density of 0.0006 particles/Å3. For the sake of clarity, the front subunit is not shown.

(B) Density map of the ligand poses of *cis*-Glyght (conformer M) obtained in the blind docking with the $\alpha_{1Z}$GlyR cryo-EM structure (Du et al., 2015), which represents an open state. Each contour line corresponds to a number density of 0.0006 particles/Å3. For the sake of clarity, the front subunit is not shown.

(C) Density map of the ligand poses of *trans*-Glyght (conformers M and P) obtained in the blind docking of the $\alpha_{2Z}$GlyR homology model (open state). Each contour line corresponds to a number density of 0.0006 particles/Å3. For the sake of clarity, the front subunit is not shown.

(D) Density map of the ligand poses of *cis*-Glyght (conformer M) obtained in the blind docking of the $\alpha_{2Z}$GlyR homology model (open state). Each contour line corresponds to a number density of 0.0006 particles/Å3. For the sake of clarity, the front subunit is not shown.

(E) ECD/TMD interface involved in the allosteric coupling between ligand binding to the ECD and opening of the ion channel pore in the TMD (Andersen et al., 2011; Bartos et al., 2009; Bertozzi et al., 2016; Cederholm et al., 2009; Jaiteh et al., 2016). Highly conserved amino acid residues throughout pGLICs (Jaiteh et al., 2016), and residues whose mutations (either in natural variants or site-directed mutagenesis experiments) affect channel activation and conductance (Lynch et al.,

1997; Ryan et al., 1994) are shown in ball and sticks colored in white (C atoms), blue (N atoms) and red (O atoms).
(F) Molecular modeling results, where the five α1ZGlyR subunits are colored in white and represented in ribbons, and the most populated poses obtained in the flexible docking of *cis*-(violet) and *trans*-Glyght (blue) in $\alpha_{1Z}$GlyR are represented in ball and sticks. Glyght binds preferentially at a non-glycine site located at the interface of the extracellular and transmembrane domains (ECD and TMD) that is involved in the allosteric coupling between ligand binding to the ECD and opening of the ion channel pore in the TMD (Andersen et al., 2011; Bertozzi et al., 2016; Cederholm et al., 2009; Jaiteh et al., 2016; Wulff et al., 2009).
(G) Detailed view of the intersubunit site at the ECD/TMD interface including the protein loops changing conformation upon receptor activation (Du et al., 2015). Interactions of the M2-M3 loop with the β8-β9 and β1-β2 loops are associated with stabilization of the closed (purple arrow) and open (blue arrow) states, respectively (Du et al., 2015). *Cis*-Glyght links the M2-M3 and β8-β9 loops, thus favouring the closed state (purple arrow). These results are in full agreement with stronger inhibition of GlyRs observed for *cis*-Glyght in panels abc.

The optogenetic control of excitatory and inhibitory circuits is defined genetically based on available cell-specific promoters (Kim et al., 2017). Photoswitchable receptor-selective drugs are powerful complementary tools that enable spatiotemporal control over pharmacologically defined circuits (glutamatergic, cholinergic, GABAergic, glycinergic) and cast new light on classical systems neuroscience research and drug-based therapies. We have used a zebrafish behavioral assay, electrophysiological analysis of receptors of known subunit composition and in brain-stem slices, and photo-response score to identify the first GlyR-selective, light-regulated inhibitor. Glyght loses inhibitory activity at saturating glycine concentrations, which is compatible with orthosteric or allosteric antagonism (Changeux and Christopoulos, 2017) (Figures S2C, S2D, S2F, and S2G). Molecular modeling results indicate that Glyght binds to an allosteric site at the interface between the ECD and the TMD that regulates GlyR gating and conductance (Andersen et al., 2011; Bertozzi et al., 2016; Cederholm et al., 2009; Jaiteh et al., 2016; Lynch et al., 1997; Ryan et al., 1994; Wulff et al., 2009) (Figure 4). This resembles the molecular switch mechanism of proline *trans*-*cis* isomerization at the ECD/TMD interface in the 5-HT3R, which has been proposed as a potential, although still controversial, mediator for channel gating (Crnjar et al., 2019; Lummis et al., 2005). Even though the interface region is highly conserved throughout Cys-loop receptors, one of the residues involved in Glyght binding ($\alpha_1$ and $\alpha_2$, T70) is present only in GlyRs (Figure 4), which may explain the selectivity of the photoswitchable compound.

Thus, Glyght also provides a template to design new allosteric nonphotoswitchable ligands like amide, ether, or methoxy analogs bearing general pharmacological interest. Glyght reversibly elicits excitatory behaviors in zebrafish larvae and is a good candidate for studying glycinergic neurotransmission in spatiotemporally defined patterns and for exploring therapeutic approaches based on localized and selective activation of GlyRs. The partial activity of Glyght in 5-$HT_{3A}$Rs is consistent with tropisetron's effect in both receptors (Yang et al., 2007) and anticipates moderate emetic activity. However, its high selectivity with respect to nicotinic receptors makes Glyght remarkably superior to strychnine (Kuijpers et al., 1994), raising hopes of modulating GlyRs without concomitant toxicity and opening a new avenue for clinical pharmacology at large.

## STAR★Methods

### Key Resources Table

| REAGENT or RESOURCE | SOURCE | IDENTIFIER |
|---|---|---|
| **Chemicals, Peptides, and Recombinant Proteins** | | |
| Glyght | This paper | N/A |

| REAGENT or RESOURCE | SOURCE | IDENTIFIER |
|---|---|---|
| Lipofectamine 3000 Transfection reagent | ThermoFisher Scientific | Cat# L3000001 |
| HEPES | Sigma-Aldrich | H3375 CAS 7365-45-9 |
| BAPTA, Tetrapotassium | ThermoFisher Scientific | Cat# B1204 |
| DMSO | Sigma-Aldrich | D8418 CAS 67-68-5 |
| GABA | Sigma-Aldrich | A2129 CAS 56-12-2 |
| Glycine | Sigma-Aldrich | G2879 CAS 6000-43-7 |
| 5-HT | Sigma-Aldrich | H9523 CAS 153-98-0 |
| Ham's F12 nutrient mixture | FisherScientific | Cat# 15172529 |
| Fetal bovine serum | FisherScientific | Cat# 11543407 |
| PenStrep | FisherScientific | Cat# 11548876 |
| L-glutamine | FisherScientific | Cat# 15430614 |
| (-)-Bicuculline methochloride | Tocris | Cat#0131 |
| Strychnine | Sigma-Aldrich | Cat#45661 |
| 6-cyano-7-nitroquinoxaline-2,3-dione (CNQX) disodium salt | Hello Bio | Cat#HB0205 |
| 2-amino-5-phosphonopentanoic acid (APV) | Hello Bio | Cat#HB0225 |
| Adenosine 5-triphosphate magnesium salt | Sigma-Aldrich | Cat#A9187 |
| Phosphocreatine disodium salt hydrate | Sigma-Aldrich | Cat#P7936 |
| Guanosine 5-triphosphate sodium salt hydrate | Sigma-Aldrich | Cat#G8877 |
| Ethylene glycol bis(2-aminoethyl ether)-N,N,N',N'-tetraacetic acid (EGTA) | Fluka analytical | Cat#03779 |
| 2-aminopyridine | Sigma Aldrich | CAS: 504-29-0 |
| Dimethylsulfide | Sigma Aldrich | CAS: 75-18-3 |
| N-Chlorosuccinimide | Sigma Aldrich | CAS: 128-09-6 |
| Sodium methoxide | Alfa Aesar | CAS: 124-41-4 |
| Borane dimethyl sulfide complex, solution 2.0 M in THF | Sigma Aldrich | CAS: 13292-87-0 |
| Thionylchloride | Merck | CAS: 7719-09-7 |
| 2-Amino-5-nitrobenzophenone | Sigma Aldrich | CAS: 1775-95-7 |
| Fmoc-Gly-OH | FluoroChem | CAS: 29022-11-5 |
| Tin(II)chloride dihydrate | Sigma Aldrich | CAS: 10025-69-1 |
| Bis(trimethylsilyl)acetylene | Acros | CAS: 14630-40-1 |
| (Trimethylsilyl)-diazomethane, solution 2.0 M in hexanes | Sigma Aldrich | CAS: 18107-18-1 |
| Sodium nitrite | Merck | CAS: 7632-00-0 |

| REAGENT or RESOURCE | SOURCE | IDENTIFIER |
|---|---|---|
| Trifluoroacetic acid | Merck | CAS: 76-05-1 |
| Sulfanilic acid | Merck | CAS: 121-57-3 |
| Tetrabutylammoniumhydroxide 30-hydrate | Sigma Aldrich | CAS: 147741-30-8 |
| Oxone, monopersulfate compound | Sigma Aldrich | CAS: 70693-62-8 |
| Sulfanilamide | Merck | CAS: 63-74-1 |
| Triethylamine | Merck | CAS: 121-44-8 |
| **Experimental Models: Cell Lines** | | |
| CHO-K1 | ATCC | Cat# CCL-61, RRID:CVCL_0214 |
| **Experimental Models: Organisms/Strains** | | |
| *Danio rerio* Tüpfel Long Fin | Parc de Recerca Biomèdica de Barcelona | AAALAC center |
| **Recombinant DNA** | | |
| plasmid GlyR alpha1 human | Taleb and Betz, 1994 | N/A |
| plasmid GlyR alpha1 mouse | Matzenbach et al., 1994 | N/A |
| plasmid GlyR beta mouse | Oertel et al., 2007 | N/A |
| plasmid GlyR alpha1 zebrafish | Devingnot et al., 2003 | N/A |
| plasmid GlyR alpha2 zebrafish | Imboden et al., 2001 | N/A |
| plasmid 5HT3A subunit | Simonin et al., 2012 | N/A |
| plasmids GABA alpha1, beta2, gamma2 subunits | Seergeeva et al., 2010 | N/A |
| **Software and Algorithms** | | |
| PatchMaster | HEKA Electronic | RRID:SCR_000034 |
| IgorPro 6.02 | WaveMatrics | RRID:SCR_000325 |
| Origin 9.0, OriginPro 2015 | OriginLabs | RRID:SCR_014212 |
| Microsoft Excel 2016 | Microsoft | RRID:SCR_016137 |
| Psfgen 1.6.4 | Gullingsrud et al., 2006 | https://www.ks.uiuc.edu/Research/vmd/plugins/psfgen/ |
| VMD 1.9.2 | Humphrey Dalke Schulten, 1996 | https://www.ks.uiuc.edu/Research/vmd/ |
| SwissModel | Waterhouse et al., 2018 | https://swissmodel.expasy.org/ |
| Avogadro 1.1.1 | Hanwell et al., 2012 | https://avogadro.cc/ |
| Gaussian 09 | Frisch et al., 2013 | https://gaussian.com/glossary/g09/ |

| REAGENT or RESOURCE | SOURCE | IDENTIFIER |
|---|---|---|
| Autodock Vina 1.1.2 | Trott and Olson, 2010 | http://vina.scripps.edu/ |
| Volmap | Cohen et al., 2006 | https://www.ks.uiuc.edu/Research/vmd/plugins/volmapgui/ |
| Binana | Durrant and McCammon, 2011 | https://sourceforge.net/projects/binana/ |
| UCSF Chimera | Pettersen et al., 2004 | https://www.cgl.ucsf.edu/chimera/ |
| GraphPad Prism 6.04 | GraphPad Software | https://www.graphpad.com |
| ZebraLab and ZebraBox | ViewPoint Life Sciences, Inc. | http://www.viewpointlifesciences.com |

## Resource Availability

### Lead Contact

Further information and requests for resources and reagents should be directed to and will be fulfilled by the Lead Contact, Pau Gorostiza (pau@icrea.cat).

### Materials Availability

All unique/stable reagents generated in this study are available from the Lead Contact with a completed Materials Transfer Agreement.

### Data and Code Availability

The datasets/code supporting the current study have not been deposited in a public repository because data from chemical library is being considered for commercial purposes but are available from the corresponding author on request.

## Experimental Model and Subject details

### CHO Cell

*In vitro* testing of the compound was performed using a line of Chinese hamster ovary (CHO-K1) cells (ATCC, Cat# CCL-61, RRID:CVCL_0214) that were transiently transfected with cDNA of different subunits of GABAA and GlyRs, and $5HT_3$ARs. CHO-K1 cells were cultured in Ham's F12 nutrient mixture supplemented with 10% fetal bovine serum, 1% of L-glutamine and 1% of penicillin/streptomycin (all from FisherScientific) at $37^0$C, 5% $CO_2$.

Commercial drugs were obtained from Sigma-Aldrich (France). Stock solutions of Glyght (10mM) and picrotoxin (50mM) were prepared using DMSO and then diluted to the final concentration in extracellular solution. Stock solutions of GABA (1M), glycine (1M) and 5HT (10mM) were prepared using MilliQwater. Non-saturating and saturating concentrations of GABA and glycine were chosen accordingly to the agonist EC50 value for the given receptor. Mean GABA $EC_{50}$ for α1/β2/γ2 $GABA_A$ receptors was determined to be 8 μM (n = 6); mean glycine $EC_{50}$ for α1Z GlyRs was 35 μM (Figure S5G, n = 6), for $\alpha_{2Z}$ 70 μM (Figure S5G; n = 6); for $\alpha_1\beta$ – 73μM (n = 9), $\alpha_2\beta$ – 130 μM (n = 9). Thus, non-saturating concentration of GABA was 5 μM, of glycine – 20 μM for $\alpha_1$, 50 μM for $\alpha_2$, 30 μM for $\alpha_1\beta$ and 100 μM for $\alpha_2\beta$. Saturating concentration for $GABA_A$ was 300 μM, for $\alpha_1$ and $\alpha_2$ GlyRs – 300 μM and 500 μM of glycine respectively.

### Mice

For electrophysiological recordings on the brain slices of mice, experiments were performed on laboratory ICR outbreed mice of both sexes at postnatal days 2–6. Use of animals was carried out in accordance with the Guide for the Care and Use of Laboratory Animals (NIH Publication No. 85–23, revised 1996) and European Convention for the Protection of Vertebrate Animals used for Experimental and other Scientific Purposes (Council of Europe No. 123; 1985). All animal protocols and experimental procedures were approved by the Local Ethics Committee of Kazan State Medical University (N_742.13.11.84 and N_1045-72). Mice had free access to food and water and were kept under natural day length fluctuations for all treatment groups. Subjects were not involved in any previous procedures. Glyght was used at the concentration of 100 μM, freshly prepared from the 50 mM stock solution dissolved in dimethyl sulfoxide (DMSO). Bicuculline, 10 μM (Tocris), strychnine, 0.2 μM (Sigma-Aldrich), 6-cyano-7-nitroquinoxaline-2,3-dione (CNQX) disodium salt, 10 μM (Hello Bio), 2-amino-5-phosphonopentanoic acid (APV), 40 μM (Hello Bio) were diluted from the 2000x stocks. All stocks were kept at -20°C.

### Electrophysiological Recordings of End-Plate Potentials in NMJ

Experiments were performed on white laboratory ICR outbred mice of both sexes of 1-3 months age. Diaphragm muscle with the attached phrenic nerve was isolated from mouse and mounted to experimental chamber. Preparation was perfused continuously with an aerated physiological saline solution (mM): NaCl - 125; KCl – 2.5; $CaCl_2$ –2; $NaH_2PO4$ – 1; $MgCl_2$ – 1; glucose – 11. The pH of solution was adjusted to 7.3 at 20°C. To prevent muscle contraction following nerve stimulation, the muscles were transversely dissected 1 hour before experiment. Intracellular recording of end-plate potentials (EPPs) was done with sharp glass microelectrodes (4–9 MΩ) using Axoclamp 900A electrophysiological amplifier (Molecular Devices, CA, USA). The motor nerve was stimulated with electrical pulses of supra-threshold amplitude and 0.1 - 0.2 ms duration with Digitimer DS3 stimulator. EPPs were recorded at low frequency stimulation of motor nerve (0.2 Hz). The resting membrane potential (RMP) of the muscle fiber was monitored through the entire experiment; those experiments that showed significant drop of RMP were not analyzed.

### Danio Rerio

Wild-type zebrafish embryos (Tüpfel long-fin strain) were purchased from the animal facility of the Barcelona Biomedical Research Park (PRBB) and raised in darkness for 6 days at 28.5 °C in UV filtered tap water in Petri dishes (daily cleaned and refilled). All animal groups were maintained under the same husbandry conditions. Animal development was checked every 24 hours. Unhealthy or abnormal embryos and larvae were removed and euthanatized in tricaine methanosulfonate 0.02%. All experiments and procedures were conducted according to the European Directive 2010/63/EU.

## Method Details

### Chemistry and Photochromism

7-aminonitrazepam (2) (Guandalini et al., 2008; Severino et al., 2008) and the nitroso derivatives 1a (Birkofer and Franz, 1971), 1b (Priewisch and Rück-Braun, 2005), 1c (Runtsch et

al., 2015), and 1d (Taylor et al., 1982)were synthesized according to reported procedures. Commercial reagents and starting materials were purchased from Acros Organics, Alfa-Aesar, Fisher Scientific, Sigma Aldrich or VWR and used without any further purification. Solvents were used in p.a. quality and dried according to common procedures, if necessary. Commercially phosphate buffer (pH = 7.4) was used for investigations of the photochromic properties. Dry nitrogen was used as inert gas atmosphere. A BiotageIsolera flash purification system with UV/Vis detector using Sigma Aldrich MN silica gel 60 M (40–63 µm, 230–400 mesh) for normal phase or pre-packed Biotage SNAP cartridges (KP C18 HS) for reversed phase chromatography was used for automated flash column chromatography. Reaction monitoring via TLC and determination of Rf values was accomplished on alumina plates coated with silica gel (Merck silica gel 60 F254, 0.2 mm). Melting points were measured with a Stanford Research Systems OptiMelt MPA 100 device and are uncorrected. NMR spectra were measured on BrukerAvance 300 ($^{1}$H 300.13 MHz, $^{13}$C 75.48 MHz), BrukerAvance 400 ($^{1}$H 400.13 MHz, $^{13}$C 100.61 MHz) and BrukerAvance III 600 ($^{1}$H 600.25 MHz, $^{13}$C 150.95 MHz) instruments. The spectra are referenced against the NMR-solvent (DMSO-d6: dH = 2.50 ppm) and the chemical shifts δ are reported in ppm. Resonance multiplicity is abbreviated as: s (singlet), d (doublet), t (triplet), q (quartet), m (multiplet) and b (broad). Carbon NMR signals are reported using DEPT135 and $^{1}$H-$^{13}$C HSQC spectra with (+) for primary/tertiary, (-) for secondary and (q) for quaternary carbons. An Agilent Q-TOF 6540 UHD (ESI-MS) instrument was used for recording mass spectra. UV/Vis absorption spectroscopy was accomplished using a Varian Cary Bio 50 UV/Vis spectrometer in 10 mm quartz cuvettes. IR-spectra were recorded on an Agilent Cary 630 FT-IR spectrometer and the peak positions are reported in wavenumbers ($cm^{-1}$). Analytical HPLC measurements were performed on an Agilent 1220 Infinity LC (column: Phenomenex Luna 3 µM C18(2) 100 Å, 150 x 2.00 mm; flow: 0.3 mL/min at 30 °C; solvent A: MilliQ water with 0.05% vol TFA; solvent B: MeCN). The ratios at the photostationary states (PSSs) were determined by HPLC measurements with a detection wavelength at the isosbestic point. For determination of the thermal half-lives the solutions were irradiated until the photostationary state was reached. Then the solutions were left at 25 °C and the recovery of the absorbance of the trans-isomer at $\lambda_{max}$ was measured. Consequently, the thermal half-life was calculated by fitting the data with a single exponential function. An Agilent 1260 system (column: Phenomenex Luna 10 µM C18(2) 100 Å, 250 x 21.2 mm; flow: 22.0 mL/min; solvent A: MilliQ water with 0.05% vol TFA; solvent B: MeCN) was used for preparative HPLC purification. Light sources for illumination were: λ = 365 nm (Herolab hand-held lamp UV-6 L, 6 W), λ = 455 nm (OSRAM Oslon SSL 80 LED, 700 mA, 1.12 W), and λ = 530 nm (CREE-XP green, 700 mA, 3.7 W). The power of the light is given based on the specifications supplied by the company when the lamps were purchased. Final compounds for biological testing possess a purity ≥95% determined by HPLC measurements with detection at 220 nm and 254 nm.

**(*E*)-7-((1*H*-pyrazol-4-yl)diazenyl)-5-phenyl-1,3-dihydro-2*H*-benzo[*e*][1,4]diazepin-2-one (3a)**

4-Nitroso-1*H*-pyrazole (1a, 71mg, 0.73mmol, 1.2eq.)was added to a solution of amino-benzodiazepine (2, 153mg, 0.61mmol, 1.0 eq.) in glacial acetic acid (8mL). Then the mixture was stirred 3days at room temperature, quenched by adding a saturated aqueous solution of $NaHCO_3$ (30mL) and diluted with EtOAc (30 mL). After separation of the layers, the aqueous layer was extracted with EtOAc (3x20mL). The combined organic layers were dried over $Na_2SO_4$, filtered and the solvent was removed under reduced pressure. Purification by preparative HPLC (15% - 45% MeCN in 25min, tR= 18.8min) afforded the desired product (30mg, 15%) as yellow solid. Rf 0.55 (CH2Cl2/MeOH 9:1); m.p. 133°C; 1H-NMR (600MHz, DMSO-d6) δ = 13.21 (bs, 1H), 10.86 (s, 1H), 8.22 (bs, 2H), 7.98 (dd, J = 8.7, 2.3 Hz, 1H), 7.56 (d, J = 2.3 Hz, 1H), 7.55 – 7.51 (m, 3H), 7.48 – 7.43 (m, 2H), 7.39 (d, J = 8.8 Hz, 1H), 4.21 (s, 2H); 13C-NMR (151MHz, DMSO-d6) δ = 170.0 (q), 169.7 (q), 158.1 (+), 157.9 (+), 146.7 (q), 141.2 (q), 140.8 (q), 138.6 (q), 130.6 (+), 129.4 (+), 128.4 (+), 126.4 (q), 125.0 (+), 124.4 (+), 122.2 (+), 56.9 (−); IR (neat) v = 3138, 2866, 1707, 1674, 1614, 1487, 1439, 1394, 1346, 1200, 1133, 995, 839,

798, 723 cm-1; HRMS (ESI) calculated. for C18H15N6O (M+H)+ m/z = 331.1302; found 331.1303.

**(*E*)-4-((2-Oxo-5-phenyl-2,3-dihydro-1H-benzo[e][1,4]diazepin-7-yl)diazenyl)benzenesulfonic acid (9) (3b)**

A 1:1 mixture of tetrabutylammonium 4-nitrosobenzenesulfonate (1b) and its corresponding nitro derivative (236mg, 0.54mmol, 1.0eq. of nitroso compound) was added to a solution of amino benzodiazepine (2, 68mg, 0.27mmol, 1.0eq.) in acetic acid (2mL) and $CH_2Cl_2$ (1mL). After stirring the mixture for 24h at room temperature the solvent was removed in vacuo. Purification by automated flash column chromatography ($CH_2Cl_2$/MeOH, 3% - 25% MeOH) and subsequent preparative HPLC (2% - 65% MeCN in 10min, $t_R$= 7.2min) yielded 3b (69mg, 61%) as yellow solid. $R_f$ 0.03 ($CH_2Cl_2$/MeOH 9:1); m.p. 280°C (decomposition); $^1$H-NMR (600MHz, DMSO-$d_6$) δ = 11.32 (s, 1H), 8.23 (dd, *J* = 8.8, 2.4 Hz, 1H), 7.81– 7.78 (m, 2H), 7.77 – 7.73 (m, 3H), 7.68 (t, *J* = 7.4 Hz, 1H), 7.64 (dd, *J* = 8.3, 1.3 Hz, 2H), 7.57 (t, *J* = 7.7 Hz, 2H), 7.52 (d, *J* = 8.9Hz, 1H), 4.34 (s, 2H); $^{13}$C-NMR (151MHz, DMSO-d6) δ = 172.5 (q), 168.9 (q), 151.4 (q), 151.1 (q), 146.5 (q), 143.0 (q), 135.8 (q),132.5 (+), 130.7 (+), 128.8 (+), 128.6 (+), 126.8 (+), 126.2 (+), 124.4 (q), 122.9 (+), 122.2 (+), 54.6 (−); IR (neat) v = 3489, 3135, 2930, 1715, 1614, 1484, 1435, 1387, 1342, 1230, 1163, 1115, 1029, 1006, 846, 742, 697 cm$^{-1}$; HRMS (ESI) calculated. for $C_{22}H_{16}N_4O_4S$ $(M+H)^+$ m/z = 421.0965; found 421.0964.

**(*E*)-4-((2-Oxo-5-phenyl-2,3-dihydro-1H-benzo[*e*][1,4]diazepin-7-yl)diazenyl)benzene-sulfonamide (3c)**

Freshly prepared 4-nitrosobenzenesulfonamide (3c, 238mg, 1.38mmol, 3.0eq.) was added to a solution of amino benzodiazepine trifluoroacetate salt (168mg, 0.46mmol, 1.0eq.) in $CH_2Cl_2$ (6mL) and acetic acid (2mL). After stirring the mixture for 24h at 40 °C the solvent was removed *in vacuo*. The residue was purified by automated flash column chromatography ($CH_2Cl_2$/MeOH, 3%-10% MeOH) yielding 3c (140mg, 73%) as orange solid. Material for analytical characterization as well as for biological testing was further purified by preparative HPLC (10% - 75% MeCN in 18 min, $t_R$ = 11.1 min). $R_f$ 0.14 ($CH_2Cl_2$/MeOH 97:3); m.p. 207 °C; $^1$H-NMR (400 MHz, DMSO-$d_6$) δ = 11.08 (s, 1H), 8.16 (dd, J = 8.8, 2.3 Hz, 1H), 7.98 (s, 4H), 7.79 (d, J = 2.3 Hz, 1H), 7.58 – 7.46 (m, 8H), 4.27 (s, 2H); 13C-NMR (101 MHz, DMSO-d6) δ = 170.1 (q), 169.8 (q), 153.2 (q), 146.2 (q), 146.0 (q) 143.0 (q), 138.0 (q), 131.1 (q), 129.7 (+), 128.5 (+), 127.8 (+), 127.1 (+), 126.1 (q), 124.9 (+), 123.0 (+), 122.6 (+), 56.5 (−); IR (neat) v = 3243, 3071, 1700, 1674, 1610, 1484, 1390, 1334, 1200, 1163, 1014, 902, 842, 798, 746, 697 cm$^{-1}$; HRMS (ESI) calculated. for $C_{21}H_{18}N_5O_3S$ (M+H)+ m/z = 420.1133; found 420.1125.

**(*E*)-5-Phenyl-7-(pyridin-2-yldiazenyl)-1,3-dihydro-2H-benzo[e][1,4]diazepin-2-one (3d) (Glyght)**

2-Nitrosopyridine (1d, 108 mg, 1.00 mmol, 2.0 eq.) was added to a solution of amino-benzodiazepine (2, 126 mg, 0.50 mmol, 1.0 eq.) in $CH_2Cl_2$ (3 mL) and acetic acid (1 mL). After stirring the mixture for 24 h at room temperature the solvent was removed *in vacuo*. The residue was purified by automated reversed phase flash column chromatography (MeCN/$H_2O$ with 0.05% TFA, 5% - 100% MeCN) and subsequent preparative HPLC (10% - 60% MeCN in 20 min, $t_R$ = 13.4 min) yielding Glyght (125 mg, 73%) as yellow solid. $R_f$ 0.63 (CH2Cl2 + 1% $Et_3N$/MeOH 9:1); m.p. 222 °C; $^1$H-NMR (600 MHz, DMSO-$d_6$) δ = 10.98 (s, 1H), 8.67 (ddd, *J* = 4.7, 1.8, 0.8 Hz, 1H), 8.17 (dd, *J* = 8.7, 2.3 Hz, 1H), 8.00 (ddd, *J* = 8.1, 7.4, 1.8 Hz, 1H), 7.79 (d, *J* = 2.2 Hz, 1H), 7.68 (dt, *J* = 8.0, 1.0 Hz, 1H), 7.56 – 7.51 (m, 4H), 7.48 – 7.44 (m, 3H), 4.25 (s, 2H); 13C-NMR (151 MHz, DMSO-$d_6$) δ = 170.1 (q), 169.3 (q), 162.6 (q), 149.4 (+), 146.1 (q), 143.0 (q), 138.9 (+), 138.8 (q), 130.5 (+), 129.3 (+), 128.4 (+), 126.8 (+), 126.7 (q), 125.8 (+), 125.1 (+), 122.4 (+), 113.3 (+), 57.2 (−); IR (neat) v = 3105, 3058, 2930, 2881, 1707, 1610, 1487, 1424,

1327, 1245, 1174, 1111, 936, 846, 790, 753, 701 $cm^{-1}$; HRMS (ESI) calculated. for $C_{20}H_{16}N_5O$ $(M+H)^+$ m/z = 342.1349; found 342.1358.

## In Vitro Studies

### Cell Culture and Ion Channel Expression

Cells were plated on 14 mm cover slips, placed inside of 35 mm cell culture dishes, one day prior to transfection (Maleeva et al., 2015; Mukhtarov et al., 2013). Transfection was performed with Lipofectamine 3000 (Life Technology, USA). The following receptor combinations were investigated during this study: $\alpha_1$ zebrafish and $\alpha_2$ zebrafish homomeric GlyRs, $\alpha_1$ human and $\alpha_2$ mouse homomeric GlyRs, $\alpha_1$ human/β mouse and $\alpha_2$ mouse/β mouse heteromeric GlyRs; heteromeric $GABA_A$Rs formed by human α1/β2/γ2 subunits. Identification of transfected cells was assured by simultaneous transfection of cDNA of green fluorescent protein (GFP); $\alpha_1$ subunit of $GABA_A$ receptor contained GFP as part of the construct. Electrophysiological recordings were performed in the fluorescent cells 24-72 hours after transfection.

### Electrophysiological Recordings in Cell Lines

Whole-cell patch-clamp recordings were held at room temperature (20–25oC) using an EPC-9 amplifier (HEKA Elektronik, Germany). Cells were continuously superfused with external solution containing (mM): NaCl 140, $CaCl_2$ 2, KCl 2.8, $MgCl_2$ 4, HEPES 20, glucose 10; pH 7.4; 320-330 mOsm. Intracellular solution used for filling recording patch pipettes contained (mM): KCl - 140, $MgCl_2$ - 2, MgATP - 2, BAPTA (tetrapotassium salt) - 2; pH 7.3 at 20°C; 290 mOsm. Pipettes were pulled from borosilicate glass capillaries (Harvard Apparatus Ltd, USA) and had resistances of 5-10 MOhm. For the rapid replacement of the solutions, the fast application system was used. Three parallel rectangular tubes (100 x 100μm) were positioned 40-50 μm above the recorded cell. The movement of the tubes was controlled by a computer-driven fast exchange system (SF 77A Perfusion Fast-Step, Warner, USA) allowing a 10–90% solution exchange in 3–5 ms, as measured by open electrode controls (1/10 external solution/water). Cells with low input resistance (<150 MOhm) and a rapid run-down (>30% with repetitive application) were excluded from analysis. UV illumination was provided by computer-driven 365nm LED (Thorlabs), positioned 5 cm above the recorded cell, the power of UV light was reaching 0.6mW/$mm^2$ at the level of recording chamber, as determined using an optical power meter (Thorlabs). Electrophysiological recordings were performed with PatchMaster (HEKA Electronic, Germany) software.

### Electrophysiology in Neuromuscular Junction (NMJ)

Diaphragm muscle with the attached phrenic nerve was isolated from mouse and mounted to experimental chamber. Preparation was perfuse continuously with an aerated physiological saline solution (mM): NaCl - 125; KCl – 2.5; $CaCl_2$ –2; $NaH_2PO_4$ – 1; $MgCl_2$ – 1; glucose – 11. The pH of solution was adjusted to 7.3 at 20°C. To prevent muscle contraction following nerve stimulation, the muscles were transversely dissected 1 hour before experiment. Intracellular recording of end-plate potentials (EPPs) was done with sharp glass microelectrodes (4 - 9 MΩ) using Axoclamp 900A electrophysiological amplifier (Molecular Devices, CA, USA). The motor nerve was stimulated with electrical pulses of supra-threshold amplitude and 0.1-0.2 ms duration with Digitimer DS3 stimulator. EPPs were recorded at low frequency stimulation of motor nerve (0.2 Hz). The resting membrane potential (RMP) of the muscle fiber was monitored through the entire experiment; those experiments that showed significant drop of RMP were not analyzed. Electrophysiological signals were digitized at 5 μs intervals stored and

processed off-line with a PC. For analysis of EPP amplitude dynamics the first signal in recording was taken as 100 percent.

**Electrophysiological Recording on Brain Slices**

Mice were decapitated; the brainstems were removed and sliced into 350-mkm-thick sections using a tissue slicer (modelNVSLM1, World Precision Instruments). Sections were prepared in an ice-cold high K+ solution, containing (in mM): K-gluconate 120, HEPES-acid 10, Na-gluconate 15, EGTA 0.2, NaCl 4 (pH 7.2, 290–300 mOsm). After cutting, slices were placed for 10 min at room temperature in an oxygenatedwith carbogen (95% O2, 5% CO2) high magnesium artificial cerebrospinal fluid (aCSF), containing (in mM): NaCl 125, KCl 2.5, CaCl2 0.8, MgCl2 8, NaHPO4 1.25, glucose 14, NaHCO3 24 (pH 7.3–7.4, 290–300 mOsm). Before experiments slices were incubated for 1 h in a chamber filled with an oxygenated a CSF containing (in mM) NaCl 125, KCl 2.5, CaCl2 2.3, MgCl2 1.3, NaHPO4 1.25, glucose 14, NaHCO3 24 (pH 7.3–7.4, 290–300 mOsm).
Glycinergic evoked inhibitory postsynaptic currents (eIPSCs) were obtained from the motor neurons of the hypoglossal nucleus, as previously described (Petukhova et al., 2018). The DS3 Constant Current Isolated Stimulator (Digitimer) and a bipolar stimulating electrode were used for the induction of reliable eIPSCs. CNQX (10 μM), APV (40 μM) and bicuculline (20 μM) were routinely added to aCSF to block the glutamatergic and GABAergic synaptic transmission. Recording was carried out at room temperature in the whole-cell configuration with the holding potential of -70 mV using the EPC-10patch-clamp amplifier (HEKA Elektronik, Germany). Patch electrodes were filled by the intracellular solution containing (in mM): CsCl 135, MgATP 4, phosphocreatine 10, GTP 0.3, HEPES 10, EGTA 5, NaCl4 (pH 7.3; 290 mOsm). Effects of Glyght on the amplitudes of glycinergic eIPSCs were examined under illumination of aCSF by diodesemitting UV (365 nm) or blue light (455 nm) (Thorlabs).

## In Vivo Studies

**Photoswitchable Behavioral Assays**

Larvae were recorded and video analyzed using the Zebrabox and Zebralab software (ViewPoint Life Sciences). Briefly, 7 days post-fertilisation (dpf) larvae were left undisturbed for 40 minutes in 200 µL fresh UV filtered water and in darkness. Continuously, 100 µL were removed and replaced with a double concentrated treatment solution and data and video recording begun. For the first 20 - 40 minutes, larvae were kept in darkness measuring basal activity, named as the resting period (RP). From the 20th minute, 2 minutes 365 nm and 455nm light changes were applied for 3 consecutive cycles, assuring the solutions to transit between their respective *cis* and *trans* photostationary states. Illumination periods at specific wavelengths lasted for 2 minutes.

All doses for used compounds were freshly prepared prior to any experiment from a 10 mM stock solution in DMSO, diluted with UV filtered water. All stocks were kept at -20°C.

All the husbandry petri dishes were blindly mixed previous to any experiment. Larvae were also blind and randomly distributed over the different treatment groups. The replacement of 100 µL of fresh UV filtered water and the addition of a double concentrated treatment solution was optimized in order to apply the same time distribution among all treated larvae with a multichannel pipette. Each treatment had 10 – 12 random individual larvae and experiments were replicated five times with five different Tüpfel-long zebrafish batches over five non-consecutive weeks. Preparation and experimental procedures were performed during the same day time.

## Modeling Studies

### Receptor Structures

The structure of the homopentameric wild-type $\alpha_{1Z}$Gly receptor ($\alpha_{1Z}$GlyR) used was the cryo-electron microscopy structure solved in the presence of Gly (PDB entry 3JAE, corresponding to an open state (Du et al., 2015). Missing side chains and hydrogen atoms were added using the psfgen plugin (version 1.6.4 (Gullingsrud et al., 2006)) in VMD (Humphrey Dalke Schulten, 1996 ) (version 1.9.2). For $\alpha_{2H}$GlyR we constructed a homology model (UniProt code P23416-2) using SwissModel (Waterhouse et al., 2018) based on the $\alpha_{1Z}$GlyR structure (PDB entry 3JAE) as template (sequence identity = 88.6 %). At the ECD/TMD interface, $\alpha_{2H}$GlyR differs by only two residues with respect to $\alpha_{1Z}$GlyR (67-68 VT → IA).

### Glyght Ligand

The initial structures of the Glyght compound (*cis* and *trans* isomers) were created employing the program Avogadro (Hanwell et al., 2012) (version 1.1.1). For each isomer, two 1,4-diazepine ring conformations, M and P, were considered, which differ in orientation (below or above the plane, respectively) of C3 and the phenyl substituent of C5 (Richter et al., 2012). For canonical benzodiazepines that bind to the classical allosteric site of the $GABA_A$ receptor, the M conformation is the bioactive one (Richter et al., 2012) (i.e. the one that shows higher affinity for receptor). However, it is not known a priori whether Glyght would exhibit similar conformational preferences, since here we consider binding to a different receptor (GlyR) and to distinct site(s). All four ligand structures (cis/M, cis/P, trans/M and trans/P) were optimized using Density Functional Theory (Rajagopal and Callaway, 1973) (DFT), with the B3LYP functional (Stephens et al., 1994) and the 6-31++G(d,p) basis set. Calculations were performed with the Gaussian 09 (G09) program package (Frisch et al., 2013). For the trans isomer, the two conformers differ only by 0.02 kcal/mol and thus their Boltzmann populations are expected to be very similar (50.8% and 49.2% for P and M, respectively). In other words, the two conformers can be present at room temperature. In the case of the cis isomer, the M conformer is significantly more stable (by 1.5 kcal/mol) than the P conformer, and thus it is the predominant conformer (with a Boltzmann population of 92%).

Autodock Vina (Trott and Olson, 2010) (version 1.1.2) was employed for ligand-receptor docking. The maximum energy difference between the best and worst binding modes and the exhaustiveness were set to default values (3kcal/mol and 8, respectively). Instead, the maximum number of modes was increase to 20 in order to increase the docking sampling. This protocol was repeated 10 times, starting with different random seeds, so that a total number of 200 binding modes were obtained for each of the four possible conformers of Glyght (cis/M, cis/P, trans/M and trans/P). For the trans isomer, the docking poses obtained for the corresponding M and P conformations were grouped together to carry out the analysis (since the two conformers are almost isoenergetic, see above), resulting in a total of 400 docking poses were considered. For the cis isomer, the 200 docking poses obtained of each conformer were analyzed separately, and only the most populated conformer, cisM, is discussed in the text.

As the location of the putative binding site(s) for Glyght in GlyR is not known, we designed a multilevel binding site screening approach, in the spirit of reference (www.bonvinlab.org/education/HADDOCK-binding-sites/): (1) blind docking using the whole receptor as a search space, (2) information-driven docking focused on the interfacial site between the extracellular and transmembrane domains identified in (1), in order to refine the docking poses and (3) a flexible docking centred in the intersubunit site found in (2) in where the residues K292, T71, T70 (in one subunit) and S289, T70, A68, S66, P291, P201, Q202, L290,

R75, R234, F161, Y239, E69 and T71 (in the adjacent subunit) were allowed to move and adapt to the ligand poses.

## Quantification and Statistical Analysis

### Electrophysiological Analysis of Cell Lines Recordings

To obtain the concentration/response curves the amplitude of evoked currents was plotted against different concentrations of agonists and Glyght (Figure 5ghi), and fitted using a non-linear fitting routine of the Origin 7.5 software (OriginLabs, USA) with the Hill equation:

$$\text{For glycine: } I = I_{max}/(1+(EC_{50}/[A])^{nH})$$

$$\text{For Glyght: } I = I_{max}/(1+([\text{Glyght}]/IC_{50})^{nH})$$

Where *I* is the normalized current amplitude induced by the agonist at concentration [A], $I_{max}$ is a maximal current induced at given cell, $n_H$ is the Hill coefficient, $EC_{50}$ or $IC_{50}$ are the concentrations at which a half-maximum response was induced, and [Glyght] is the concentration of Glyght used in the experiment. Ionic current recordings were analyzed with Igor Pro 6.02 and Origin 9.0 software. For statistical analysis paired and unpaired t-tests were used. Data are represented as means ± SEM.

### Electrophysiological Analysis on Brain Slices

Ionic current recordings were performed and measured using PatchMaster software (HEKA Electronic). OriginPro2015 (Origin Lab), Excel 2016 (Microsoft) and Igor Pro 6.02 (WaveMetrics) software were employed to accomplish a statistical analysis of the data and to plot the graphs. Data were presented as means ± SEM. Significance of differences was assessed using paired sample Wilcoxon signed rank test. Differences were considered significant at $p < 0.05$. Further statistical details are to be found in figure legends.

### Electrophysiological Analysis on NMJ

Electrophysiological signals were recorded and analyzed using homemade software. Signals were digitized at 5 μs intervals stored and processed off-line with a PC. For analysis of EPP amplitude dynamics the first signal in recording was taken as 100 percent.

### *Danio Rerio* Behavioural Analysis

Zebrafish tracking was performed in real time and data acquisition integrated one- or two-minute intervals using the Zebralab software (ViewPoint Life Science). Data statistical analysis was performed using GraphPad Prism 6 software. Selective illumination was performed with two ordered based [evenly distributed] arrays of 12 light emitting diodes (LEDs) for each wavelength placed 12 cm afar of the multiwell plate. The light intensities, measured with an optical power meter (model Newport 1916-C), were 5.9 $W \cdot m^{-2}$ for 365 nm (UV) and 2.4 $W \cdot m^{-2}$ for 455 nm (Visible-Blue). Larvae activity was measured as the sum of fast swimming durations over one-minute integration per well (fast swimming time). Distance activity was measured as the sum of swimming distances (in millimeters) during burst activities over one-minute integration. Data were analyzed following Two-way ANOVA (p-value 0.05) and are presented as mean ± standard error of the mean (s.e.m.) with the number of larvae (n) indicated in each case. UV/Visible activity ratio (UVAR) was extracted from raw activity data as the swimming ratio between the total of six minutes of UV illumination and the total of six minutes of visible illumination for each drug treatment. Further statistical details are to be found in figure legends, both in main and Supplemental Information.

**Computational and Modeling Analysis**

The initial blind docking results were analyzed in terms of the number density of the ligand poses. Previous studies have successfully used this type of analysis to identify ligand binding sites in other ion channels (Bregestovski and Maleeva, 2019; Raju et al., 2013). The underlying assumption is that regions of continuous density (or high occupancy) should represent regions of tighter binding. The number density value was computed using the Volmap plugin (Cohen et al., 2006) of VMD (Humphrey Dalke Schulten, 1996). Namely, each Glyght position was replaced with a normalized Gaussian distribution of width equal to 1.5 Å and the Gaussians were additively distributed on a three-dimensional grid of dimensions 0.5 x 0.5 x 0.5 $Å^3$. For the information-driven docking, we analyzed the most populated pose clusters using the quality threshold algorithm implemented in VMD (https://github.com/luisico/clustering) in order to delineate the specific site within the ECD/TMD interface.(3) The flexible docking results were analyzed in terms of the interactions between the ligand and the receptor. On one hand, statistical analysis of protein residues close to the Glyght docking poses was carried out and the percentage contact frequency was calculated considering that a receptor-ligand contact is present if the protein residue is within 5 Å of Glyght. It is assumed that amino acids with high frequencies pinpoint possible binding residues. On the other hand, the representative structure of the most populated cluster(s) was analyzed using the Binana algorithm (Durrant and McCammon, 2011). The images of the modelling section were generated with either the UCSF Chimera package (Pettersen et al., 2004) or the VMD program (Humphrey Dalke Schulten, 1996).

## Acknowledgments

We are grateful to S. Lummis for the 5-HT3A subunit cDNA. This study was supported by ERA SynBIO grant MODULIGHTOR (PCIN-2015-163-C02-01), the Russian Science Foundation (grant 18-15-00313), AGAUR/Generalitat de Catalunya (CERCA Programme 2017-SGR-1442), FEDER funds, Human Brain Project WAVESCALES (SGA2 Grant Agreement 785907), Fundaluce Foundation, MINECO (Project CTQ2016-80066R), an FPI-MICIU PhD scholarship to A.M.J.G., an FI-AGAUR PhD scholarship to A.N.-H., and an IBEC-BEST postdoctoral scholarship to G.M. We also thankfully acknowledge the computer resources at MareNostrum III and MinoTauro and the technical support provided by the Barcelona Supercomputing Center (BCV-2017-2-0004). We also acknowledge the CECH project cofinanced by the European Union Regional Development Fund within the framework of the ERDF Operational Program of Catalonia 2014-2020 with a grant of 50% of total eligible cost.

## Author Contributions

A.M.J.G and X.R. performed in vivo experiments. K.R., D.W., and A.B.B. performed compound chemical synthesis and characterization. G.M., E.M., E.P., D.P., and M.M performed electrophysiological analysis. F.P. and M.B. performed in vitro experiments. A.N.H. and M.P. performed molecular modeling simulations and analysis. C.R. supervised molecular modeling. B.K. supervised chemical synthesis. P.B. conceived and supervised electrophysiological in vitro studies. P.G. conceived the project and supervised in vivo experiments. A.M.J.G. and P.G. wrote the manuscript with contributions from all authors.

## Declaration of Interests

The authors declare no competing interests.

## Supplemental Information (2)

Document S1. Figures S1–S4, Table S1, and Data S1 and S2
Document S2. Article plus Supplemental Information

# References


1. Andersen, N. · Corradi, J. · Bartos, M. ...
   Functional relationships between agonist binding sites and coupling regions of homomeric cys-loop receptors.
   J. Neurosci. 2011; 31:3662-3669

2. Bartos, M. · Corradi, J. · Bouzat, C.
   Structural basis of activation of Cys-loop receptors: The extracellular-transmembrane interface as a coupling region.
   Mol. Neurobiol. 2009; 40:236-252

3. Bencan, Z. · Sledge, D. · Levin, E.D.
   Buspirone, chlordiazepoxide and diazepam effects in a zebrafish model of anxiety.
   Pharmacol. Biochem. Behav. 2009; 94:75-80

4. Berry-Kravis, E. · Hagerman, R. · Visootsak, J. ...
   Arbaclofen in fragile X syndrome: Results of phase 3 trials.
   J. Neurodev. Disord. 2017; 9:1-18

5. Bertozzi, C. · Zimmermann, I. · Engeler, S. ...
   Signal transduction at the domain interface of prokaryotic pentameric ligand-gated ion channels.
   PLoS Biol. 2016; 14:1-25

6. Birkofer, L. · Franz, M.
   C-nitrosierungen über silyl-derivate.
   Chem. Ber. 1971; 104:3062-3068

7. Bregestovski, P.D. · Maleeva, G.V.
   Photopharmacology: a brief review using the control of potassium channels as an example.
   Neurosci. Behav. Physiol. 2019; 49:184-191

8. Burgos, C.F. · Yevenes, G.E. · Aguayo, L.G.
   Structure and pharmacologic modulation of inhibitory glycine receptors.
   Mol. Pharmacol. 2016; 90:318-325

9. Cederholm, J.M.E. · Schofield, P.R. · Lewis, T.M.
   Gating mechanisms in Cys-loop receptors.
   Eur. Biophys. J. 2009; 39:37-49

10. Changeux, J.P. · Christopoulos, A.
    Allosteric modulation as a unifying mechanism for receptor function and regulation.
    Diabetes Obes. Metab. 2017; 19:4-21

11. Chesnoy-Marchais, D.
    Potentiation of chloride responses to glycine by three 5-HT3 antagonists in rat spinal

neurones.
Br. J. Pharmacol. 1996; 118:2115-2125

12. Cohen, J. · Arkhipov, A. · Braun, R. …
Imaging the migration pathways for O2, CO, NO, and Xe inside myoglobin.
Biophys. J. 2006; 91:1844-1857

13. Crnjar, A. · Comitani, F. · Hester, W. …
Trans-cis proline switches in a pentameric ligand-gated ion channel: how they are affected by and how they affect the biomolecular environment.
J. Phys. Chem. Lett. 2019; 10:694-700

14. Cui, W.W. · Low, S.E. · Hirata, H. …
The zebrafish shocked gene encodes a glycine transporter and is essential for the function of early neural circuits in the CNS.
J. Neurosci. 2005; 25:6610-6620

15. Devingnot, V. · Prado de Carvalho, L. · Bregestovski, P. …
A novel glycine receptor αZ1 subunit variant in the zebrafish brain.
Neuroscience. 2003; 122:449-457

16. Du, J. · Lü, W. · Wu, S. …
Glycine receptor mechanism elucidated by electron cryo-microscopy.
Nature. 2015; 526:224-229

17. Durrant, J.D. · McCammon, J.A.
BINANA: a novel algorithm for ligand-binding characterization.
J. Mol. Graph. Model. 2011; 29:888-893

18. Frisch, M.J. · Trucks, G.W. · Schlegel, H.B. …
Gaussian 09, Revision D.01
Gaussian Inc., 2013 1-20

19. Gielen, M. · Thomas, P. · Smart, T.G.
The desensitization gate of inhibitory Cys-loop receptors.
Nat. Commun. 2015; 6:1-10

20. Griffin, C.E. · Kaye, A.M. · Bueno, F.R. …
Benzodiazepine pharmacology and central nervous system-mediated effects.
Ochsner J. 2013; 13:214-223

21. Guandalini, L. · Cellai, C. · Laurenzana, A. …
Design, synthesis and preliminary biological evaluation of new hydroxamate histone deacetylase inhibitors as potential antileukemic agents.
Bioorg. Med. Chem. Lett. 2008; 18:5071-5074

22. Guglielmi, G. · Barry, J.D. · Huber, W. …
An optogenetic method to modulate cell contractility during tissue morphogenesis.
Dev. Cell. 2015; 35:646-660

23. Gullingsrud, J. · Saam, J. · Phillips, J.
Psfgen User's Guide
University of Illinois and Beckman Institute, 2006

24. Hanwell, M.D. · Curtis, D.E. · Lonie, D.C. …
Avogadro: an advanced semantic chemical editor, visualization, and analysis platform.
J. Cheminform. 2012; 4:17

25. Hennermann, J.B. · Berger, J.M. · Grieben, U. ...
Prediction of long-term outcome in glycine encephalopathy: a clinical survey.
J. Inherit. Metab. Dis. 2012; 35:253-261

26. Hirata, H. · Saint-Amant, L. · Downes, G.B. ...
Zebrafish bandoneon mutants display behavioral defects due to a mutation in the glycine receptor -subunit.
Proc. Natl. Acad. Sci. U S A. 2005; 102:8345-8350

27. Huckvale, R. · Mortensen, M. · Pryde, D. ...
Azogabazine; a photochromic antagonist of the GABA A receptor.
Org. Biomol. Chem. 2016; 14:6676-6678

28. Hüll, K. · Morstein, J. · Trauner, D.
In vivo photopharmacology.
Chem. Rev. 2018; 118:10710-10747

29. Humphrey Dalke Schulten, W.A.K.
Visual molecular dyanmics.
J. Mol. Graph. 1996; 14:33-38

30. Imboden, M. · De Saint Jan, D. · Leulier, F. ...
Isolation and characterization of an alpha 2-type zebrafish glycine receptor subunit.
Neuroscience. 2001; 103:799-810

31. Izquierdo-Serra, M. · Bautista-Barrufet, A. · Trapero, A. ...
Optical control of endogenous receptors and cellular excitability using targeted covalent photoswitches.
Nat. Commun. 2016; 7:12221

32. Izquierdo-Serra, M. · Hirtz, J.J. · Shababo, B. ...
Two-photon optogenetic mapping of excitatory synaptic connectivity and strength.
iScience. 2018; 8:15-28

33. Jaiteh, M. · Taly, A. · Hénin, J.
Evolution of pentameric ligand-gated ion channels: Pro-loop receptors.
PLoS One. 2016; 11:1-24

34. Jensen, A.A. · Gharagozloo, P. · Birdsall, N.J.M. ...
Pharmacological characterisation of strychnine and brucine analogues at glycine and α7 nicotinic acetylcholine receptors.
Eur. J. Pharmacol. 2006; 539:27-33

35. Kim, C.K. · Adhikari, A. · Deisseroth, K.
Integration of optogenetics with complementary methodologies in systems neuroscience.
Nat. Rev. Neurosci. 2017; 18:222-235

36. Kimmel, C.B. · Ballard, W.W. · Kimmel, S.R. ...
Stages of embryonic development of the zebrafish.
Dev. Dyn. 1995; 203:253-310

37. Kuijpers, G.A.J. · Vergara, L.A. · Calvo, S. ...
Inhibitory effect of strychnine on acetylcholine receptor activation in bovine adrenal medullary chromaffin cells.
Br. J. Pharmacol. 1994; 113:471-478

38. Lee, G.-H. · Sung, S.-Y. · Chang, W.-N. ...
Zebrafish larvae exposed to ginkgotoxin exhibit seizure-like behavior that is relieved by pyridoxal-5'-phosphate, GABA and anti-epileptic drugs.
Dis. Model. Mech. 2012; 5:785-795

39. Li, W.-C. · Moult, P.R.
The control of locomotor frequency by excitation and inhibition.
J. Neurosci. 2012; 32:6220-6230

40. Lichtenegger, M. · Tiapko, O. · Svobodova, B. ...
An optically controlled probe identifies lipid-gating fenestrations within the TRPC3 channel article.
Nat. Chem. Biol. 2018; 14:396-404

41. Liu, Y. · Carmer, R. · Zhang, G. ...
Statistical analysis of zebrafish locomotor response.
PLoS One. 2015; 10:1-25

42. Lummis, S.C.R. · Beene, D.L. · Lee, L.W. ...
Cis-trans isomerization at a proline opens the pore of a neurotransmitter-gated ion channel.
Nature. 2005; 438:248-252

43. Lynch, J.W. · Rajendra, S. · Pierce, K.D. ...
Identification of intracellular and extracellular domains mediating signal transduction in the inhibitory glycine receptor chloride channel.
EMBO J. 1997; 16:110-120

44. Lynch, J.W. · Zhang, Y. · Talwar, S. ...
Glycine Receptor Drug Discovery
Elsevier Inc., 2017

45. MacPhail, R.C. · Brooks, J. · Hunter, D.L. ...
Locomotion in larval zebrafish: influence of time of day, lighting and ethanol.
Neurotoxicology. 2009; 30:52-58

46. Maleeva, G. · Buldakova, S. · Bregestovski, P.
Selective potentiation of alpha 1 glycine receptors by ginkgolic acid.
Front. Mol. Neurosci. 2015; 8:1-11

47. Maleeva, G. · Wutz, D. · Rustler, K. ...
A photoswitchable GABA receptor channel blocker.
Br. J. Pharmacol. 2019; 176:2661-2677

48. Matzenbach, B. · Maulet, Y. · Sefton, L. ...
Structural analysis of mouse glycine receptor alpha subunit genes. Identification and chromosomal localization of a novel variant.
J Biol Chem. 1994; 269:2607-2612

49. Menezes, C.M.S. · Rivera, G. · Alves, M.A. ...
Synthesis, biological evaluation, and structure-activity relationship of clonazepam, meclonazepam, and 1,4-benzodiazepine compounds with schistosomicidal activity.
Chem. Biol. Drug Des. 2012; 79:943-949

50. Mukhtarov, M. · Liguori, L. · Waseem, T. ...
Calibration and functional analysis of three genetically encoded Cl−/pH sensors.
Front. Mol. Neurosci. 2013; 6:1-12

51. Oertel, J. · Villmann, C. · Kettenmann, H. ...
A novel glycine receptor β subunit splice variant predicts an unorthodox transmembrane topology: Assembly into heteromeric receptor complexes.
J Biol Chem. 2007; 282:2798-2807

52. Ogino, K. · Hirata, H.
Defects of the glycinergic synapse in zebrafish.
Front. Mol. Neurosci. 2016; 9:1-18

53. Pettersen, E.F. · Goddard, T.D. · Huang, C.C. ...
UCSF Chimera--a visualization system for exploratory research and analysis.
J. Comput. Chem. 2004; 25:1605-1612

54. Petukhova, E. · Ponomareva, D. · Mukhamedyarov, M. ...
Developmental changes in the inhibition of glycinergic synaptic currents by niflumic acid in hypoglossal motoneurons.
Front. Mol. Neurosci. 2018; 11:1-9

55. Pittolo, S. · Gómez-Santacana, X. · Eckelt, K. ...
An allosteric modulator to control endogenous G protein-coupled receptors with light.
Nat. Chem. Biol. 2014; 10:813-815

56. Pittolo, S. · Lee, H. · Lladoó, A. ...
Reversible silencing of endogenous receptors in intact brain tissue using two-photon pharmacology.
bioRxiv. 2019

57. Priewisch, B. · Rück-Braun, K.
Efficient preparation of nitrosoarenes for the synthesis of azobenzenes.
J. Org. Chem. 2005; 70:2350-2352

58. Rajagopal, A.K. · Callaway, J.
Inhomogeneous electron gas.
Phys. Rev. B. 1973; 136:B864

59. Raju, S.G. · Barber, A.F. · LeBard, D.N. ...
Exploring volatile general anesthetic binding to a closed membrane-bound bacterial voltage-gated sodium channel via computation.
PLoS Comput. Biol. 2013; 9:1-10

60. Reiner, A. · Isacoff, E.Y.
Tethered ligands reveal glutamate receptor desensitization depends on subunit occupancy.
Nat. Chem. Biol. 2014; 10:273-280

61. Richter, L. · Graaf, C. De · Sieghart, W. ...
Diazepam-bound GABAA receptor models identify new benzodiazepine binding-site ligands.
Nat. Chem. Biol. 2012; 8:455-464

62. Rost, B.R. · Schneider-Warme, F. · Schmitz, D. ...
Optogenetic tools for subcellular applications in neuroscience.
Neuron. 2017; 96:572-603

63. Rudolph, U. · Crestani, F. · Möhler, H.
GABAAreceptor subtypes: Dissecting their pharmacological functions.
Trends Pharmacol. Sci. 2001; 22:188-194

64. Runtsch, L.S. · Barber, D.M. · Mayer, P. ...
Azobenzene-based inhibitors of human carbonic anhydrase II
Beilstein J. Org. Chem. 2015; 11:1129-1135

65. Ryan, S.G. · Buckwalter, M.S. · Lynch, J.W. ...
A missense mutation in the gene encoding the α1 subunit of the inhibitory glycine receptor in the spasmodic mouse.
Nat. Genet. 1994; 7:131-135

66. Schaefer, N. · Berger, A. · van Brederode, J. ...
Disruption of a structurally important extracellular element in the glycine receptor leads to decreased synaptic integration and signaling resulting in severe startle disease.
J. Neurosci. 2017; 37:7948-7961

67. Schmid, K. · Foutz, A.S. · Denavit-Saubié, M.
Inhibitions mediated by glycine and GABAA receptors shape the discharge pattern of bulbar respiratory neurons.
Brain Res. 1996; 710:150-160

68. Schnörr, S.J. · Steenbergen, P.J. · Richardson, M.K. ...
Measuring thigmotaxis in larval zebrafish.
Behav. Brain Res. 2012; 228:367-374

69. Seergeeva, O.A. · Kletke, O. · Kragler, A. ...
Fragrant dioxane derivatives identify β1-subunit-containing GABAA receptors.
J Biol Chem. 2010; 285:23985-23993

70. Severino, B. · Fiorino, F. · Perissutti, E. ...
Synthesis and pharmacological evaluation of peptide-mimetic protease-activated receptor-1 antagonists containing novel heterocyclic scaffolds.
Bioorg. Med. Chem. 2008; 16:6009-6020

71. Shemesh, O.A. · Tanese, D. · Zampini, V. ...
Publisher Correction: Temporally precise single-cell-resolution optogenetics.
Nat. Neurosci. 2017; 20:896

72. Shin, Y. · Chang, Y.C. · Lee, D.S.W. ...
Liquid nuclear condensates mechanically sense and restructure the genome.
Cell. 2018; 175:1481-1491.e13

73. Simonin, J. · Vernekar, S.K. · Thompson, A.J. ...
High-affinity fluorescent ligands for the 5-HT3 receptor.
Bioorg Med Chem Lett. 2012; 22:1151-1155

74. Stein, M. · Middendorp, S.J. · Carta, V. ...
Azo-propofols: photochromic potentiators of GABAA receptors.
Angew. Chem. Int. Ed. 2012; 51:10500-10504

75. Stephens, P.J. · Devlin, F.J. · Chabalowski, C.F. ...
Ab Initio calculation of vibrational absorption and circular dichroism spectra using density functional force fields.
J. Phys. Chem. 1994; 98:11623-11627

76. Taleb, O. · Betz, H.
Expression of the human glycine receptor alpha 1 subunit in Xenopus oocytes: apparent affinities of agonists increase at high receptor density.
EMBO J. 1994; 13:1318-1324

77. Taylor, E.C. · Tseng, C.P. · Rampal, J.B.
Conversion of a primary amino group into a nitroso group. Synthesis of nitroso-substituted heterocycles.
J. Org. Chem. 1982; 47:552-555

78. Trott, O. · Olson, A.
Autodock vina: improving the speed and accuracy of docking.
J. Comput. Chem. 2010; 31:455-461

79. Waterhouse, A. · Bertoni, M. · Bienert, S. ...
SWISS-MODEL: homology modelling of protein structures and complexes.
Nucleic Acids Res. 2018; 46:W296-W303

80. Wulff, P. · Ponomarenko, A.A. · Bartos, M. ...
Hippocampal theta rhythm and its coupling with gamma oscillations require fast inhibition onto parvalbumin-positive interneurons.
Proc. Natl. Acad. Sci. U S A. 2009; 106:3561-3566

81. Yang, Z. · Ney, A. · Cromer, B.A. ...
Tropisetron modulation of the glycine receptor: Femtomolar potentiation and a molecular determinant of inhibition.
J. Neurochem. 2007; 100:758-769

82. Yevenes, G.E. · Zeilhofer, H.U.
Allosteric modulation of glycine receptors.
Br. J. Pharmacol. 2011; 164:224-236

83. Yue, L. · Pawlowski, M. · Dellal, S.S. ...
Robust photoregulation of GABA A receptors by allosteric modulation with a propofol analogue.
Nat. Commun. 2012; 3:1012-1095

**Cell Chemical Biology, Volume *27***

## Supplemental Information

# Photocontrol of Endogenous Glycine Receptors *In Vivo*

**Alexandre M.J. Gomila, Karin Rustler, Galyna Maleeva, Alba Nin-Hill, Daniel Wutz, Antoni Bautista-Barrufet, Xavier Rovira, Miquel Bosch, Elvira Mukhametova, Elena Petukhova, Daria Ponomareva, Marat Mukhamedyarov, Franck Peiretti, Mercedes Alfonso-Prieto, Carme Rovira, Burkhard König, Piotr Bregestovski, and Pau Gorostiza**

# Supplementary Figures and Tables

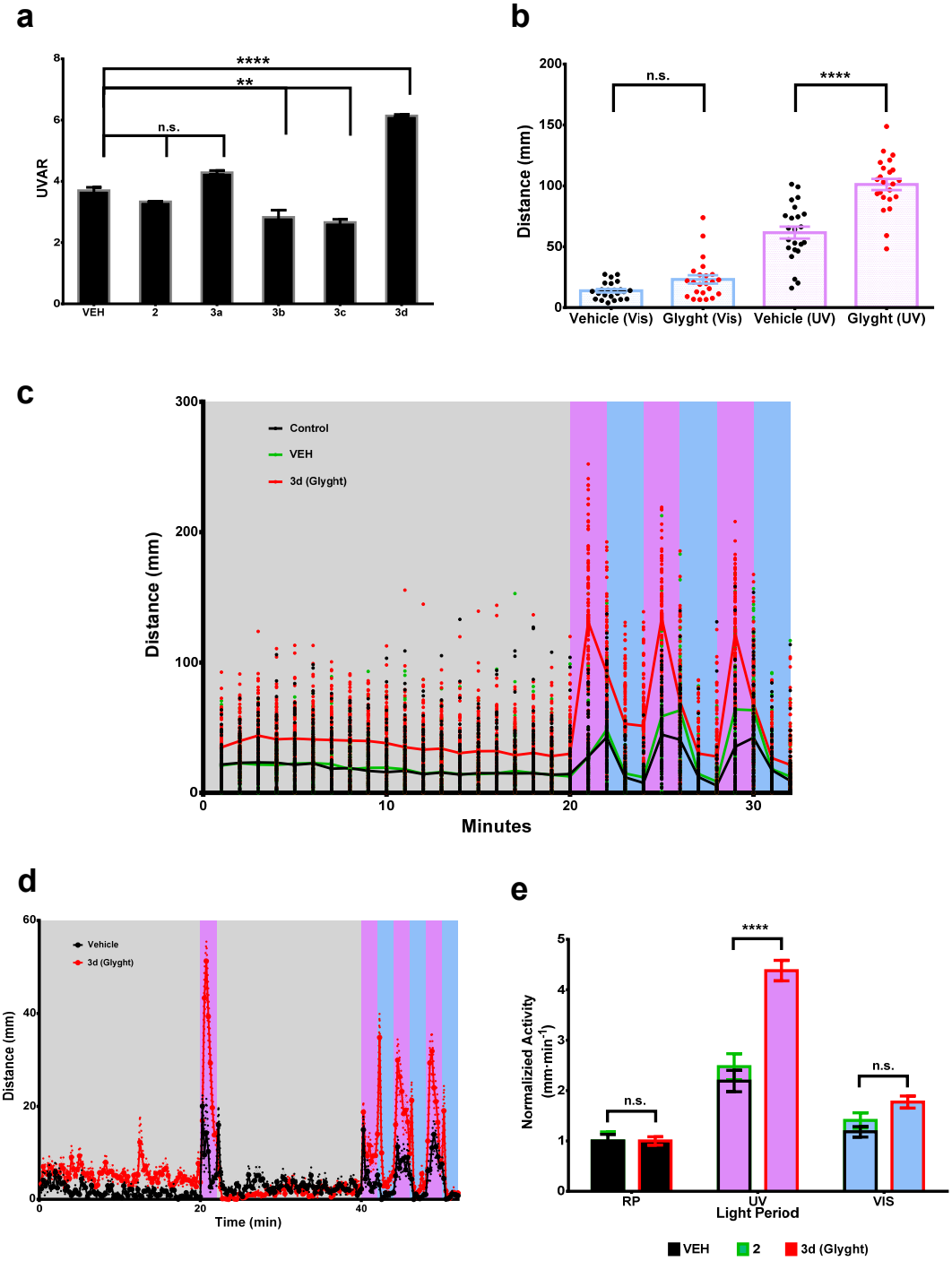


Supplementary Figure 1 related to Figure 2.

**a.** The ratio between activities during UV and visible cycles can be used as a photoswitchable behavior score. The UV/VIS activity ratio (UVAR) calculated for each compound can be compared to control UVAR (endogenous photoresponses in vehicle) and provide a simple mean to evaluate statistically the significance of the differences. Dunnet's multiple comparison test was conducted (p-value = 0.05). **3b-c** and **3d (Glyght)** were significantly different from vehicle (VEH) with p-values **p < 0.01 and ****p < 0.0001, respectively. In independent experiments, an UVAR = 3.7 ± 0.18 was consistently found in vehicle-treated 7 dpf Tüpfel-Long fin zebrafish in the described experimental conditions.

**b.** Larvae activity (mm·min$^{-1}$) over all visible and UV light periods was integrated for Vehicle and Glyght treatments (23 larvae per drug treatment). One-way ANOVA with Sidak's multiple comparison test was

conducted (p-value = 0.05). Error bars represent standard error of the mean (S.E.M.). Glyght induced a significant increase in larvae activity (p-value < 0.0001) compared to control larvae under UV light, and non-significant (n.s.) differences were found in the same larvae for visible light dependent activities.

**c.** Larvae fast movements activities were analyzed every minute ($mm \cdot min^{-1}$) in five independent experiments –Control (larvae clean water, n = 111), VEH (1% DMSO, n = 95), **2** (n = 46) and **3d** (Glyght) (n = 94). Experiments record larvae burst depending activity for 20 minutes in Dark condition (RP) followed by 3 consecutives cycles of 2 minutes 365 nm and 455 nm light exposures. Error bars represent S.E.M. for treated larvae over one-minute integration periods.

**d.** Kinetics of Glyght turning off in the dark. Fast swimming (FS, time spent swimming faster than 6 $mm \cdot s^{-1}$) of individual larvae exposed to vehicle and Glyght during RP, UV and VIS illumination was integrated into 15 seconds data points. Same burst activity for compound 3d is observed for UV illumination periods during their first minute of exposure (startle response) and a subsequent decrease. For the first UV period, larvae activity was reduced to near zero once illumination finished. Since *cis*-Glyght relaxes slowly in the dark (thermal half-life 80 min), this behavior can be due to persistent inhibition of the hindbrain network, as observed by W. W. Cui *et al.* (see reference in main text) upon glycine accumulation, which led to a decrease in zebrafish larvae motility through different larval stages (from 28 to 72 hpf) and could be recovered through pharmacological blockade of glycine action. The activity observed in our experiments (Figure 1d) is recovered during the 3 light cycles. Error bars indicate the standard deviation of the mean (S.E.M.) of FS in each bin period for vehicle (n = 8) and 3d (n = 13) individual larvae.

**e.** The fractional increase in swimming caused by Glyght and UV light is significantly higher than in the vehicle. Last minute of the RP was used to normalize the activity of each treatment under the first minute of UV and visible illumination. Vehicle (DMSO) and 2 (7-AN) –black and green border coloured bars, respectively- showed no significant differences on activity. On the other hand, 3d (Glyght, red border coloured bars) showed a significant increase of larvae motility under UV illumination but no difference was observed when visible light was applied. Two-way ANOVA with Tukey's multiple comparison test was used for the analysis were ****p < 0.0001, n.s. (not significant); n for Vehicle, 2 and 3d were 111, 46 and 94 larvae from a total of 5 independent experiments, respectively. Errors bars indicate the standard error of the mean (S.E.M.).

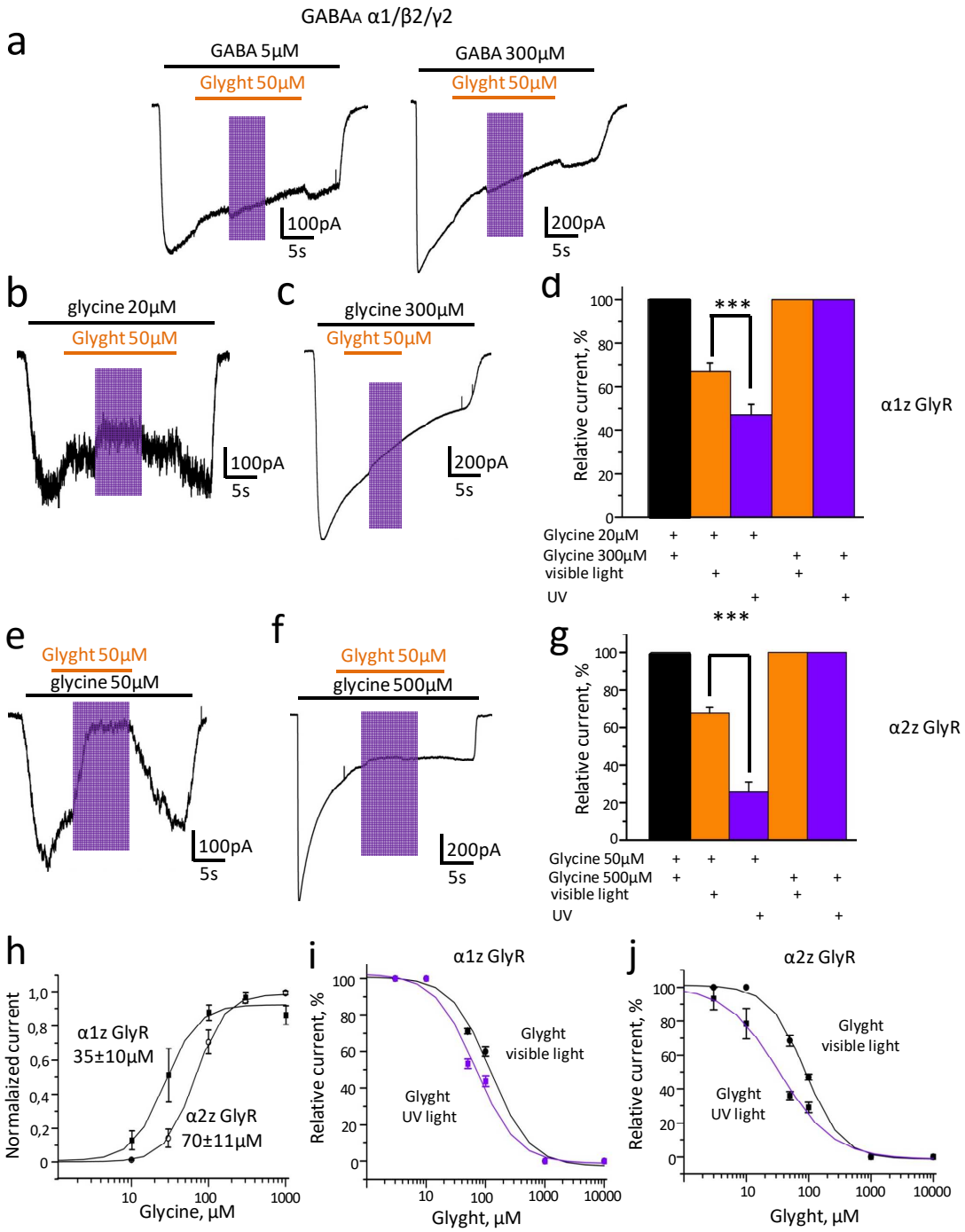


## Supplementary Figure 2, related to Figure 3.

**a.** Glyght has only a minor inhibitory effect on $GABA_AR$-mediated currents. Left: a representative recording of current induced by application of 5 μM of GABA (black bar) and by mixture of GABA with Glyght 50 μM (orange bar); UV illumination is indicated by violet rectangle. Right: a representative recording of current induced by application of 300 μM of GABA and by mixture of GABA with Glyght 50 μM; $V_{hold}$ -30 mV.

**b.** Representative recording of the $\alpha_{1Z}$-mediated current induced by application of glycine 20 μM (indicated by black bar) and by mixture of glycine 20 μM and Glyght 50 μM (indicated by orange bar); time of UV illumination indicated by violet rectangle.

**c.** Representative recording of the $\alpha_{1Z}$ current induced by 300 μM of glycine and by mixture of glycine 300 μM and Glyght 50 μM.

**d.** Relative amplitude of $\alpha_{1Z}$ currents in control (black column; 20 or 300 μM of glycine were applied), at application of the mixture of glycine with Glyght 50 μM under visible light (orange column) and mixture of glycine and Glyght 50 μM under UV light (violet column), $p \leq 0.001$, n = 8.

**e.** Representative trace of the $\alpha_{2Z}$ current induced by application of glycine 50 µM and by mixture of glycine 50 µM and Glyght 50 µM.

**f.** Representative recording of the $\alpha_{2Z}$ current induced by 500 µM of glycine and by mixture of glycine 500 µM and Glyght 50 µM.

**g.** Relative amplitude of $\alpha_{2Z}$ currents induced by application of glycine (50 or 500 µM; black column), mixture of glycine with Glyght 50 µM under visible light (orange column) and by mixture of glycine and Glyght 50 µM under UV light (violet column), $p \leq 0.001$, n = 4. For all recordings $V_{hold}$ -30mV.

**h.** Cumulative dose/response curves for glycine at $\alpha_{1Z}$ (filled squares, n = 6) and $\alpha_{2Z}$ GlyRs (empty circles, n = 6).

**i.** Cumulative dose/response curves for Glyght at $\alpha_{1Z}$ GlyRs at visible light (black curve) and upon UV illumination (violet curve); currents were induced by non-saturating concentration of glycine, n = 5.

**j.** Cumulative dose/response curves for Glyght at $\alpha_{2Z}$ GlyRs at visible light (black curve) and under UV illumination (violet curve); currents were induced by non-saturating concentration of glycine, n = 4.

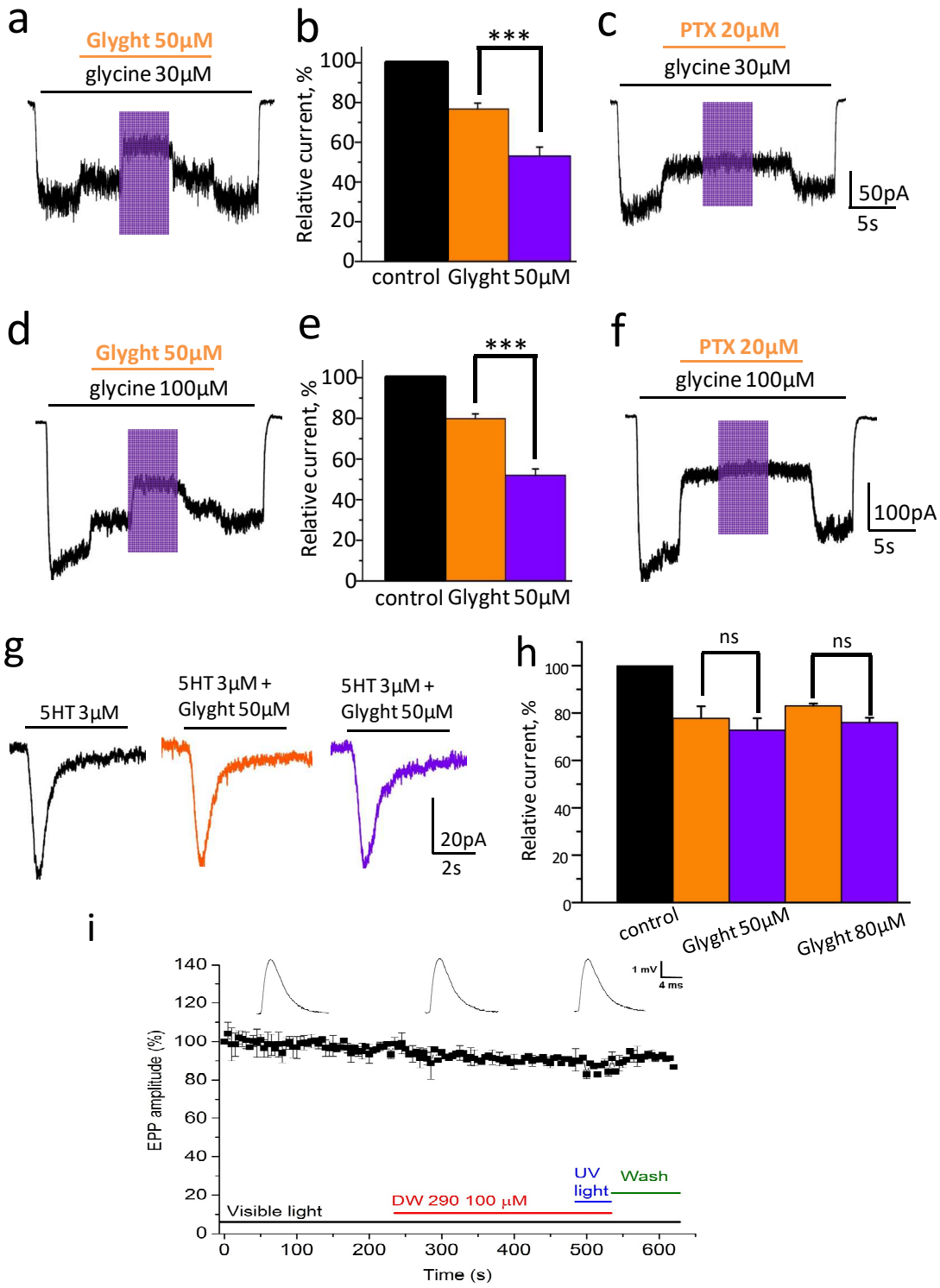


Supplementary Figure 3 related to Figure 3.

- **a.** Representative recording of α1β current induced by 30 µM of glycine and by mixture of glycine 30 µM/ Glyght 50 µM at visible and UV light.
- **b.** Relative amplitude of α1β currents in control (30 µM of glycine; black column), at application of the mixture of glycine with Glyght 50 µM under visible light (orange column) and mixture of glycine/ Glyght 50 µM under UV light (violet column), n = 7, $p \leq 0.001$.
- **c.** Representative trace of α1β current induced by glycine 30 µM and by mixture of glycine with PTX 20 µM, note the absence of the effect of UV light on the current amplitude.
- **d.** Representative recording of α2β current induced by 100 µM of glycine and by mixture of glycine 100 µM / Glyght 50 µM at visible and UV light.

**e.** Relative amplitude of α2β currents in control (100 μM of glycine; black column), at application of the mixture of glycine with Glyght 50 μM under visible light (orange column) and mixture of glycine / Glyght 50 μM under UV light (violet column), $n = 7$, $p \leq 0.001$.

**f.** Representative trace of α1/β current induced by 100 μM of glycine and by mixture of glycine with 20 μM of PTX illustrating the absence of UV light effect on PTX induced inhibition.

**g.** Representative traces of currents induced by application of 5HT 3 μM (black trace), by mixture of 5HT with Glyght 50 μM at visible light (orange trace) and by mixture of 5HT with Glyght 50 μM at UV light (violet trace).

**h.** Cumulative data on relative amplitude of 5HT-induced currents in control (black column), at application of 50 and 80 μM of Glyght at visible light (orange columns) and at application of 50 and 80 μM of Glyght at UV light (violet columns), $p > 0.05$, $n = 4$.

**i.** The effect of 100 μM of Glyght (shown by red line) on the amplitude of end-plate potentials (EPP) at the mouse neuromuscular junction when applied under the r light (shown by black line) and UV light (365 nm, shown by violet line). Glyght wash-out was done at the end of experiment (shown by green line). At the upper part of the figure are shown examples of native end-plate potential records at different moments of experiment: in control (left), during application of Glyght at visible light (middle) and at UV illumination (right).

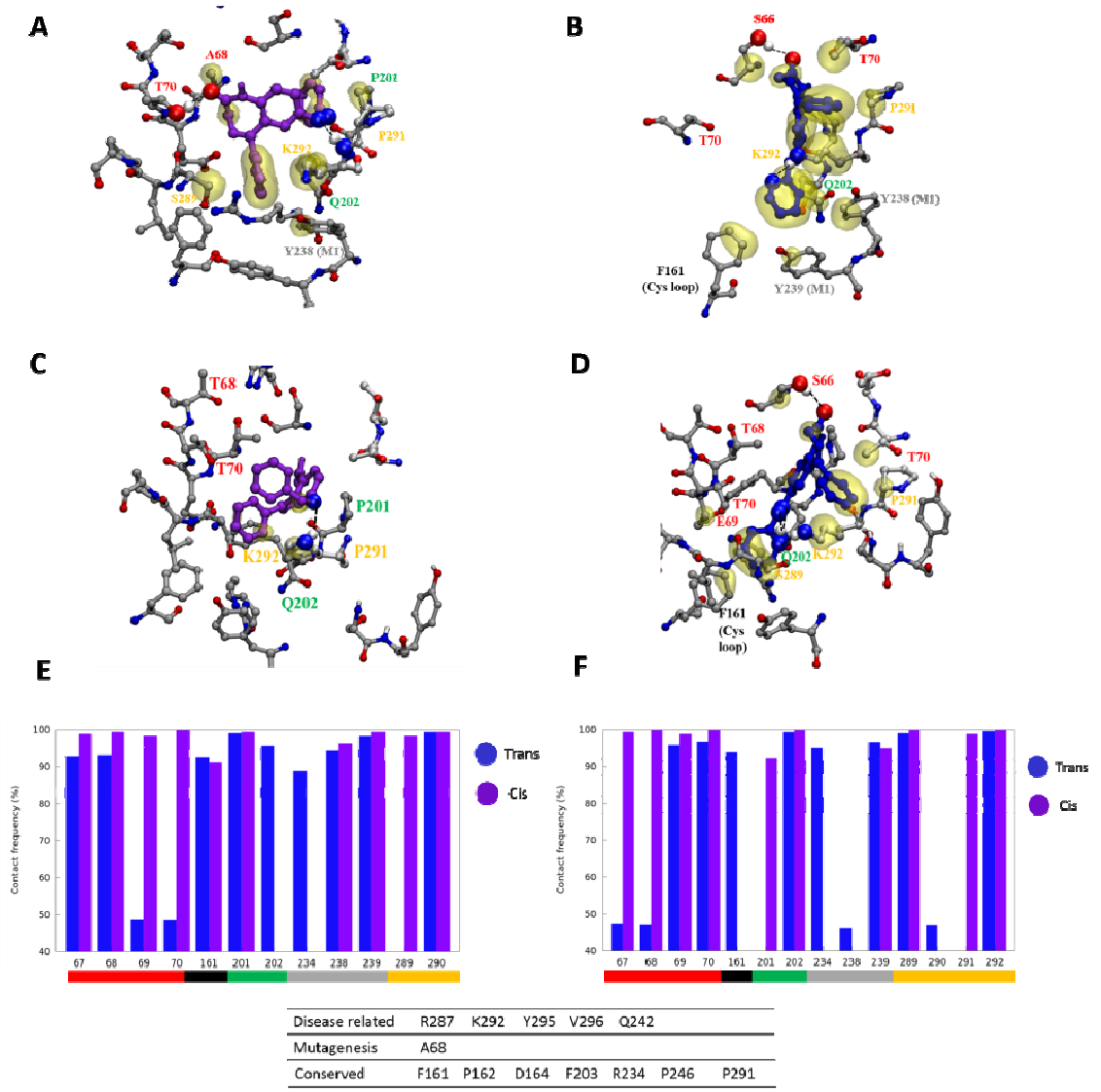


| | | | | | | | |
|---|---|---|---|---|---|---|---|
| Disease related | R287 | K292 | Y295 | V296 | Q242 | | |
| Mutagenesis | A68 | | | | | | |
| Conserved | F161 | P162 | D164 | F203 | R234 | P246 | P291 |

Supplementary Figure 4 related to Figure 4.

**a.** Detailed view of the most representative pose of *cis*-Glyght bound to the ECD/TMD interfacial site obtained in the flexible docking with $\alpha_1$GlyR. Hydrophobic contacts between *cis*-Glyght and the receptor residues are represented as a yellow surface and the atoms involved in hydrogen bonds between the ligand and Lys292 and Thr70 are represented with more voluminous balls and a dashed line. The residues in direct contact with *cis*-Glyght are indicated.

**b.** Detailed view of the most representative pose of *trans*-Glyght bound to the ECD/TMD interfacial site obtained in the flexible docking with α1 GlyR. Hydrophobic contacts between *trans*-Glyght and the receptor residues are represented as a yellow surface and the atoms involved in the hydrogen bonds between the ligand and Lys292 and Ser66 are represented with more voluminous balls and a dashed line. The residues in direct contact with *trans*-Glyght are indicated.

**c.** Detailed view of the *cis*-Glyght most probable binding site in $\alpha_2$GlyR (67-68IA → 67-68 VT). Hydrophobic contacts between *cis*-Glyght and the receptor residues are represented as a yellow surface and the atoms involved in the hydrogen bond between the ligand and Lys292 are represented with more voluminous balls and a dashed line. The residues in direct contact with *cis*-Glyght are indicated.

**d.** Detailed view of the *trans*-Glyght most probable binding site in α2 GlyR. Hydrophobic contacts between *trans*-Glyght and the receptor residues are represented as a yellow surface and the atoms involved in the hydrogen bonds between the ligand and Lys292, Gln202 and Ser66 are represented with more voluminous balls and a dashed line. The residues in direct contact with *trans*-Glyght are indicated.

**e.** Percentage of the frequency that a residue is closer than 5Å with Glyght in α1 GlyR. In blue the *trans*-Glyght isomer and in violet, *cis*-Glyght. A coloured box below the residues numbers indicates to which loop they belong; red, black, green, grey and yellow correspond to β1-β2, Cys, β8-β9, preM1-M1 and M2-M3 loops, respectively.

**f.** Percentage of the frequency that a residue is closer than 5Å with Glyght in α2 GlyR. In blue the *trans*-Glyght isomer and in violet, *cis*-Glyght. A coloured box below the residue numbers indicates to which loop

they belong; the same colour code as in panel (e) is used. The highly conserved residues in the pGLICs family and the residues whose mutation affects negatively the channel activity and conductance are listed in the table below.

## Supplementary Table 1 related to Figure 1.

Photochemical properties of substituted azobenzene benzodiazepine derivatives **3 a-d**.

| Entry | Cpd | Conc. [µM] | solvent | $\lambda_{max}$*trans* [nm] | $\lambda_{max}$*cis* [nm] | $t_{1/2}$(25 °C) [h] | PSS[*,a]*cis* [%] | PSS[*,b]*trans* [%] |
|---|---|---|---|---|---|---|---|---|
| **1** | **3a** | 50 | DMSO | 350 | none | 2.7 h | 88 | 71 |
| **2** | **3a** | 50 | PBS + 0.1% DMSO | 339 | none | - [c] | n.d. | n.d. |
| **3** | **3b** | 50 | DMSO | 361 | 440 | 17.4 | 88 | 82 |
| **4** | **3b** | 50 | PBS + 0.1% DMSO | 347 | 429 | 55.6 | n.d. | n.d. |
| **5** | **3c** | 50 | DMSO | 365 | 442 | 21.1 | 88 | 82 |
| **6** | **3c** | 50 | PBS + 0.1% DMSO | 348 | 427 | 30.4 | n.d. | n.d. |
| **7** | **3d** | 50 | DMSO | 357 | 435 | 7.8 | 80 | 84 |
| **8** | **3d** | 50 | PBS + 0.1% DMSO | 348 | 425 | 1.4 | n.d. | n.d. |

n.d.: not determined; [*] determined by HPLC measurements; [a] PSS at photoconversion from the *trans* to the *cis* isomer; [b] PSS at photoconversion from the *cis* to the *trans* isomer; [c] could not be determined due to decomposition or precipitation after 5 h in PBS solution.

# Data S1 related to Method details in STAR Methods.

## Compound 3a

Detection at 220 nm: $t_R$ = 10.8 min; 98 %

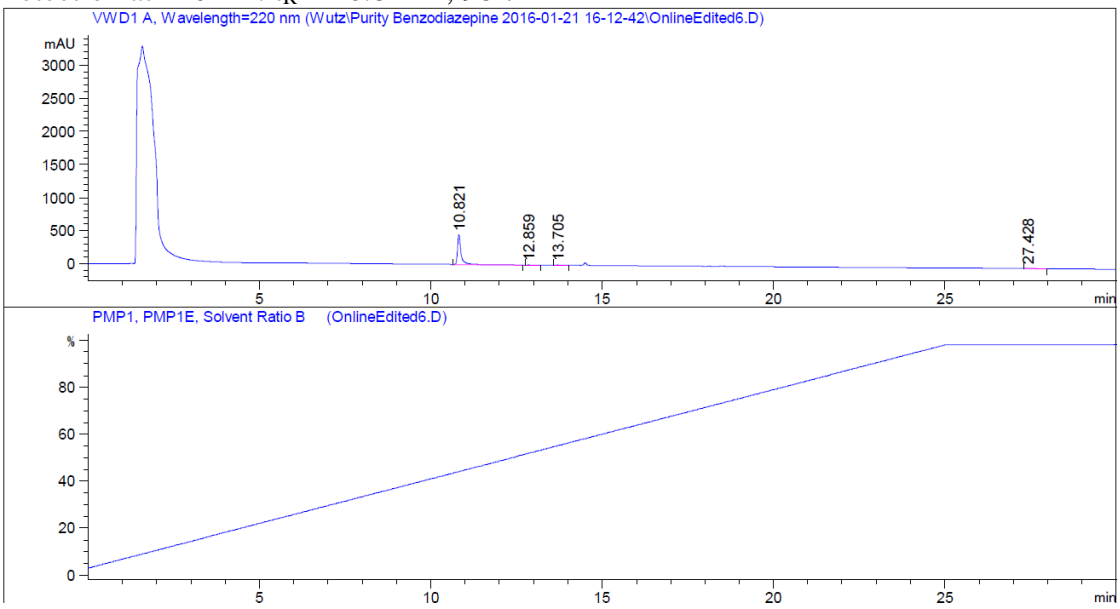


Detection at 254 nm: $t_R$ = 10.8 min; 100 %

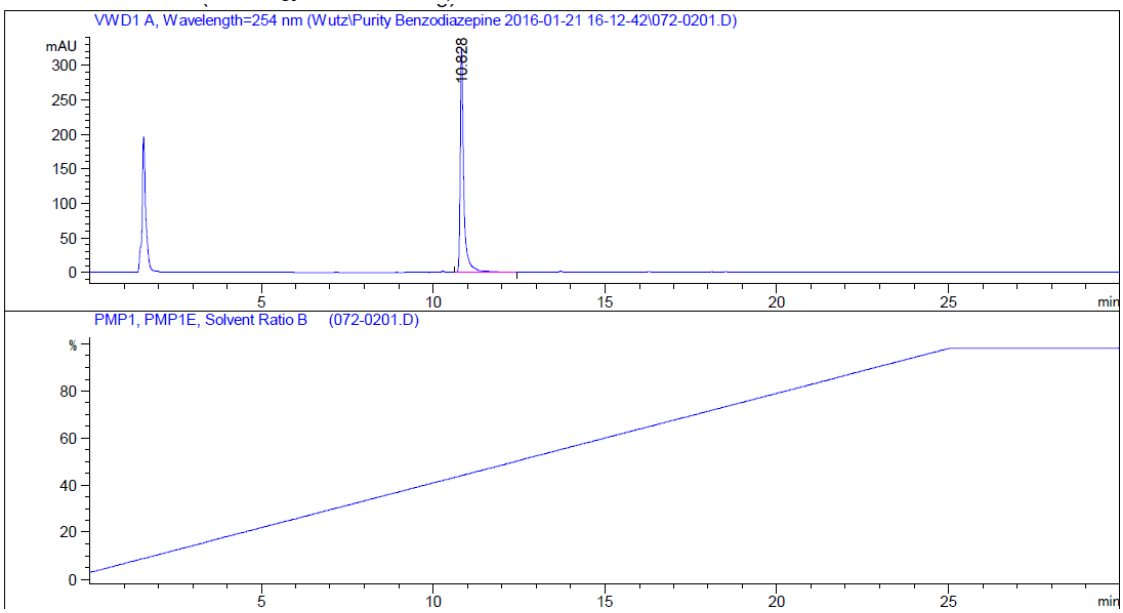

## Compound 3b

Detection at 220 nm: $t_R$ = 9.8 min; 98 %

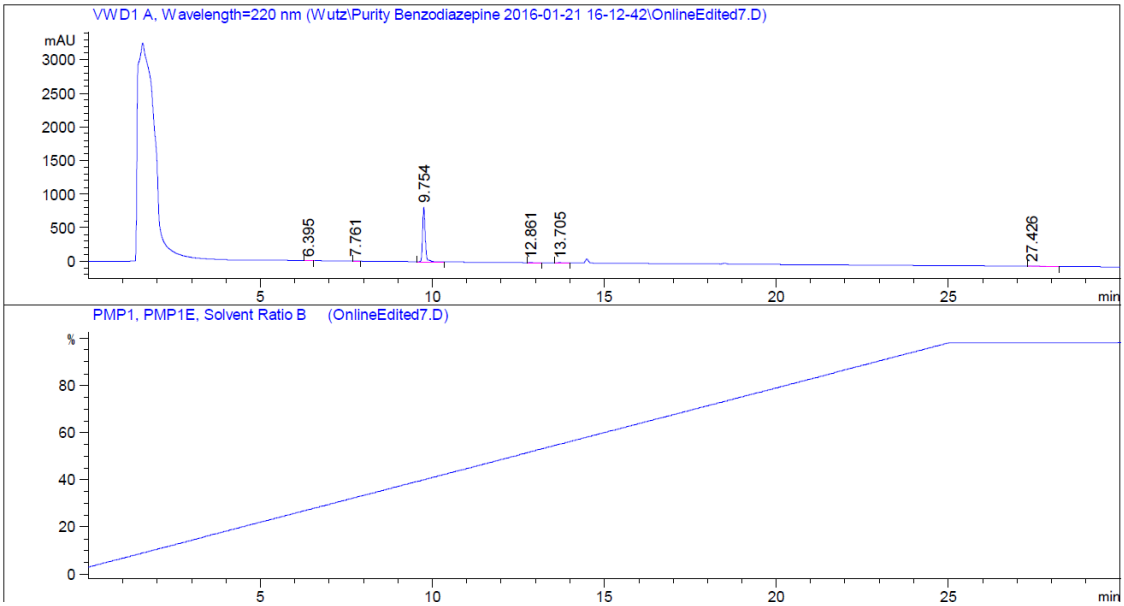


Detection at 254 nm: $t_R$ = 9.8 min; 98 %

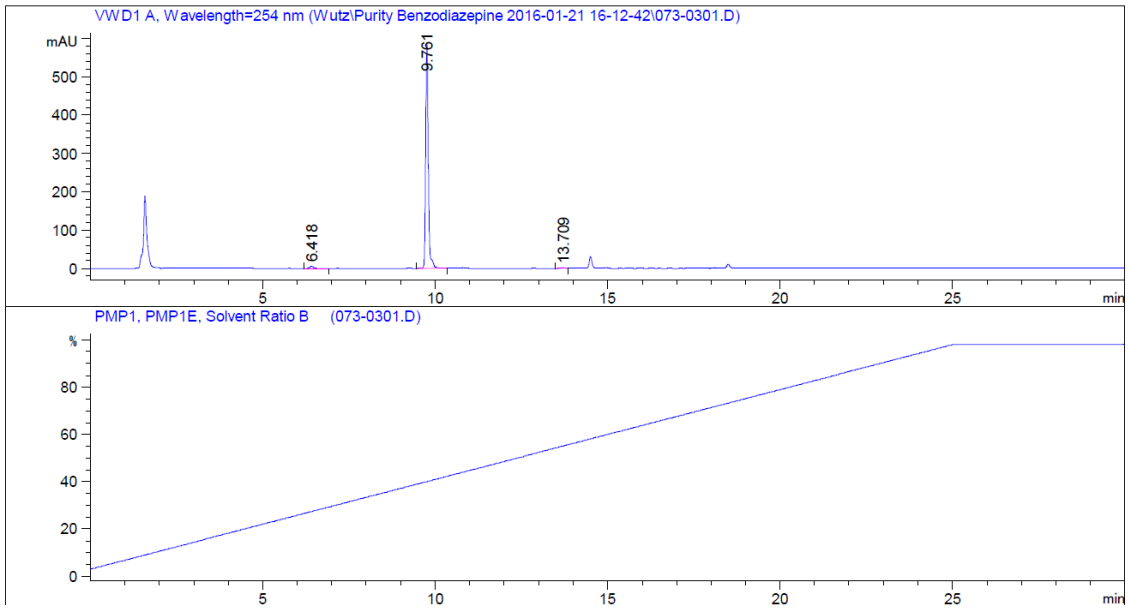

## Compound 3c

Detection at 220 nm: $t_R$ = 13.0 min; 98 %

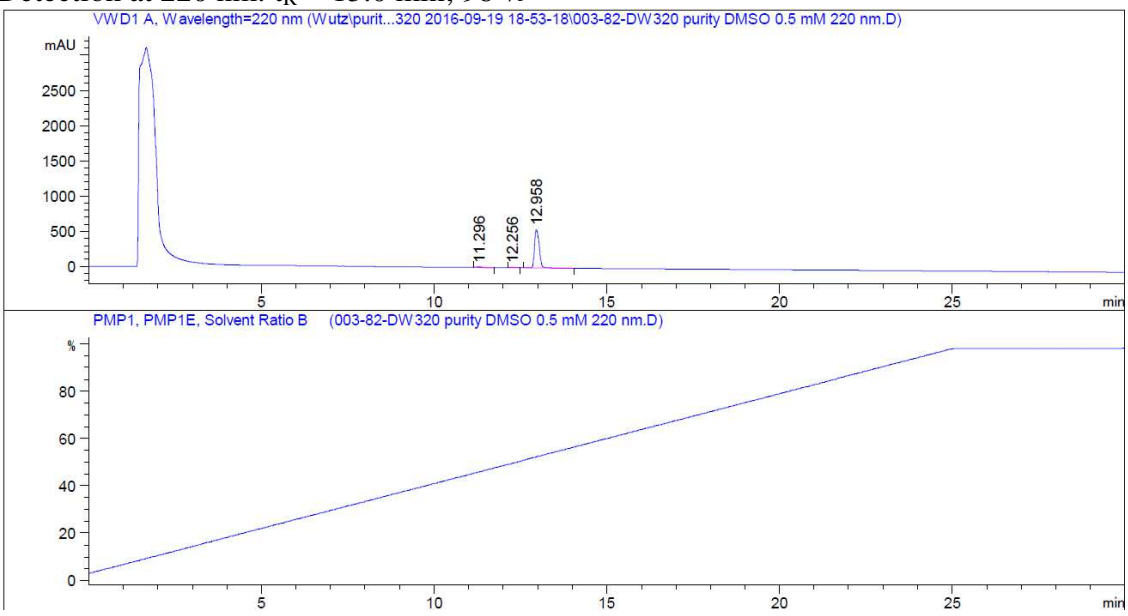


Detection at 254 nm: $t_R$ = 13.0 min; 96 %

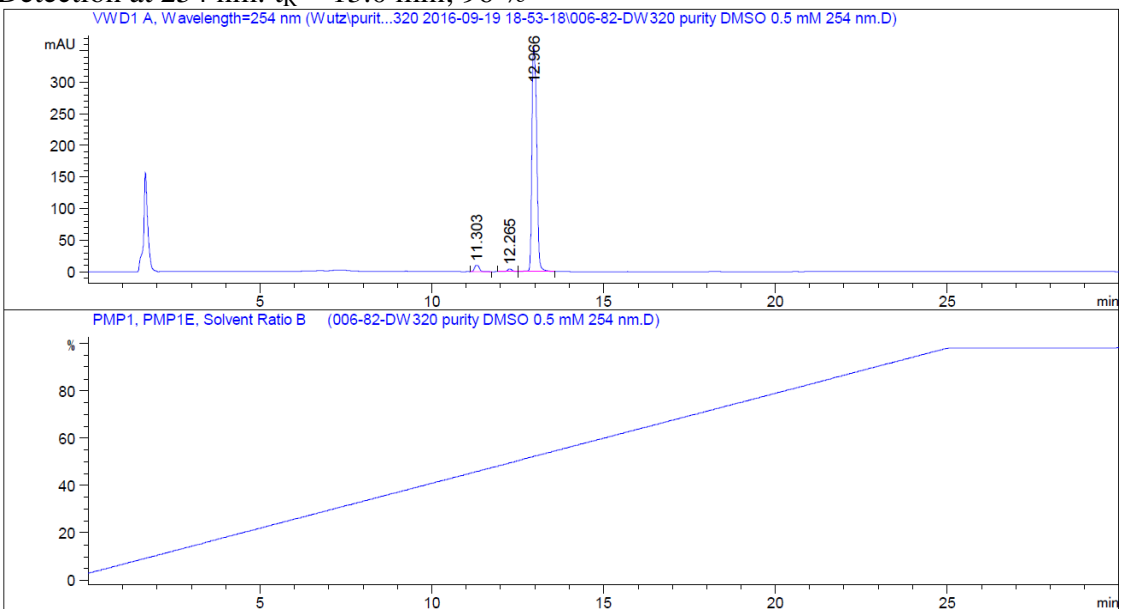

## Compound 3d

Detection at 220 nm: $t_R$ = 13.1 min; 99 %

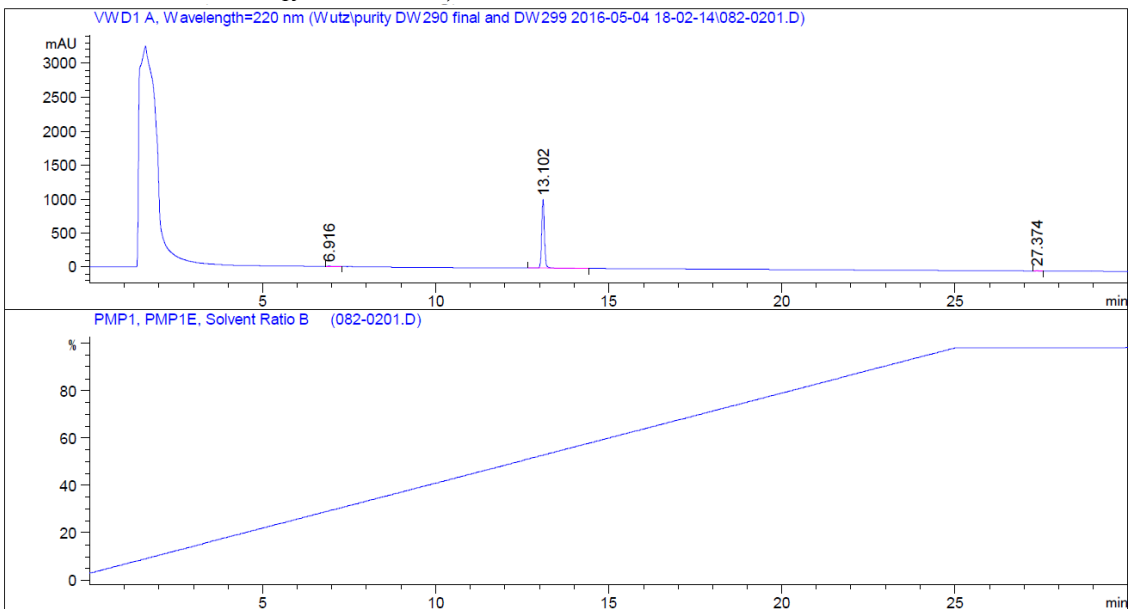


Detection at 254 nm: $t_R$ = 13.1 min; 95 %

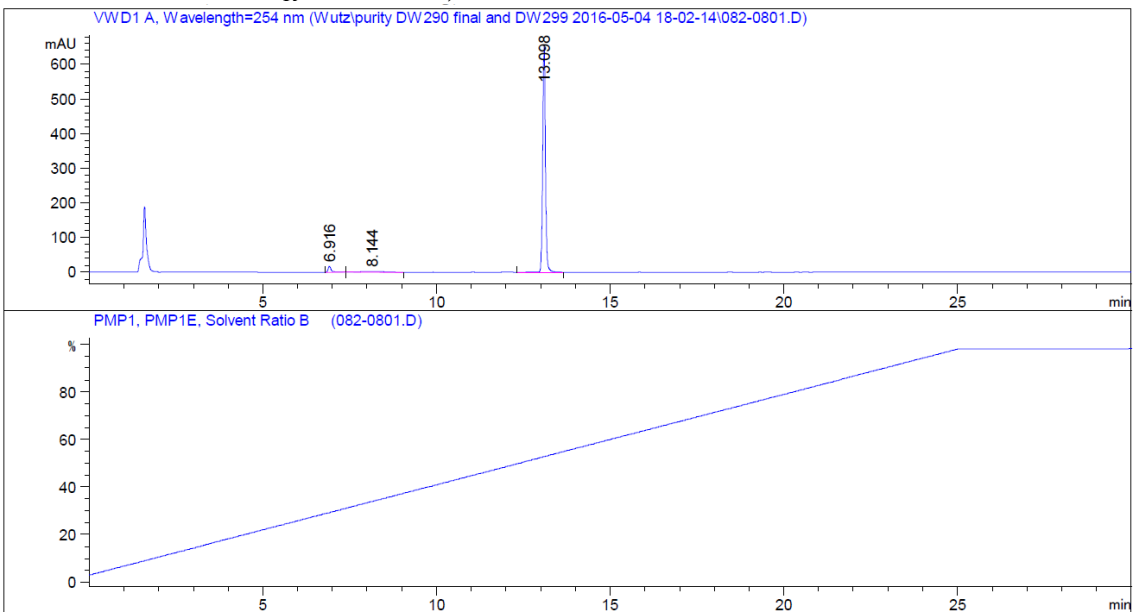

# Data S2 related to Method details in STAR Methods. $^{1}H$- and $^{13}C$-NMR spectra

## Compound 3a

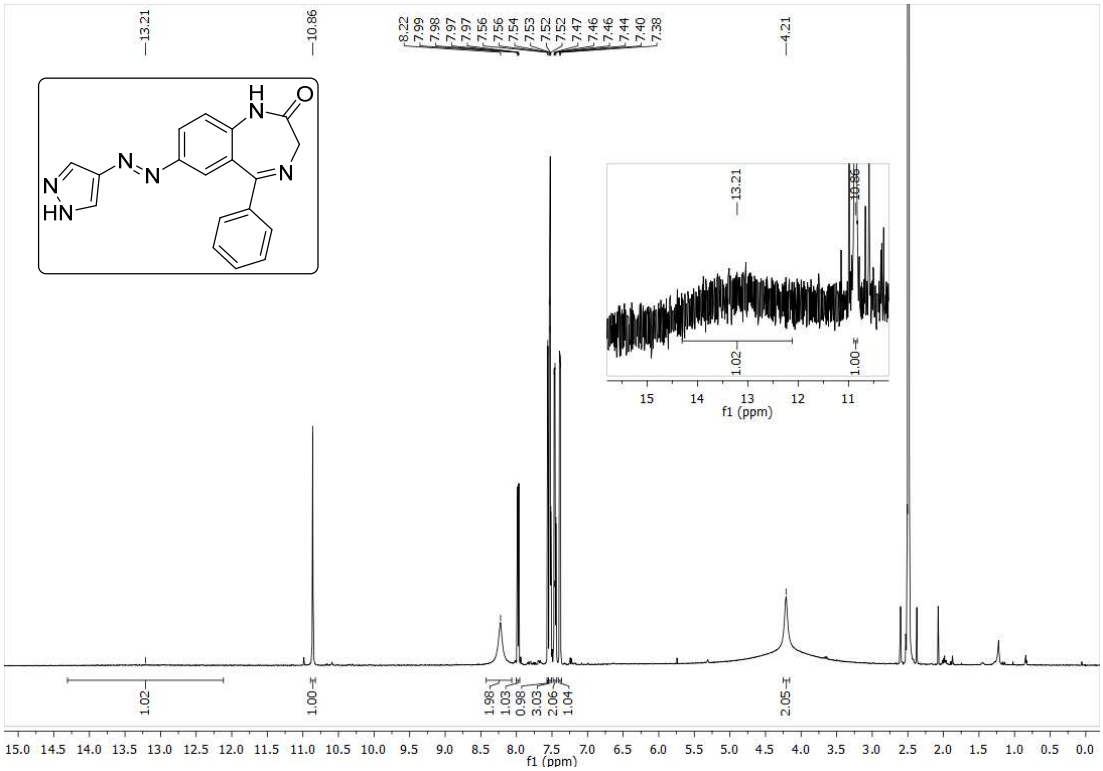


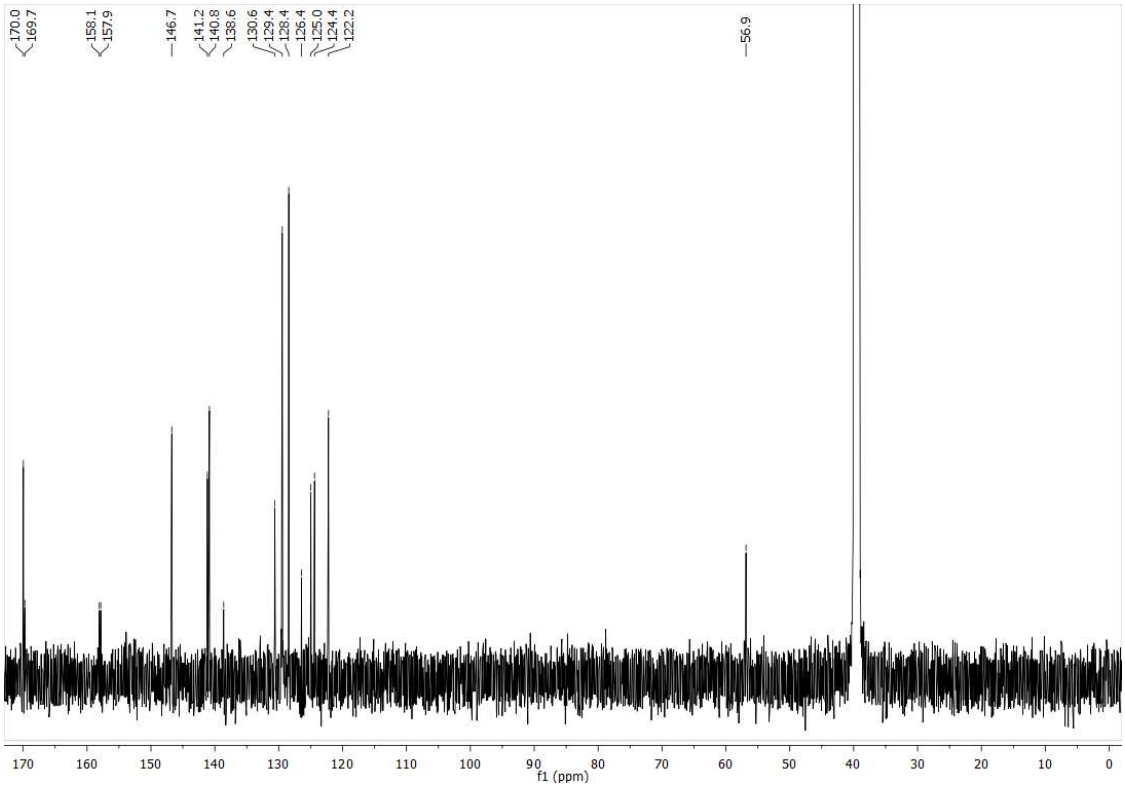

## Compound 3b

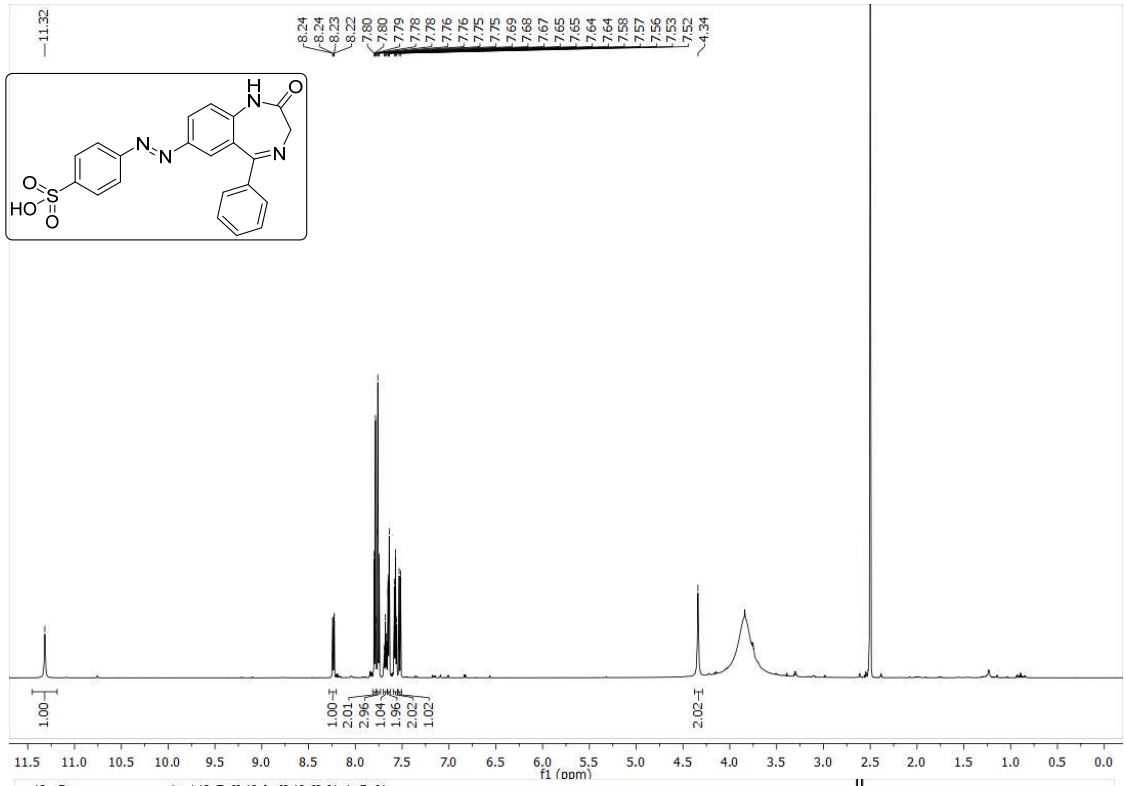
11.32
8.24
8.24
8.23
8.22
7.80
7.80
7.79
7.78
7.78
7.76
7.76
7.75
7.75
7.69
7.68
7.67
7.65
7.65
7.64
7.64
7.58
7.57
7.56
7.53
7.52
4.34
1.00
1.00
2.01
2.96
1.04
1.96
2.02
1.02
2.02
11.5 11.0 10.5 10.0 9.5 9.0 8.5 8.0 7.5 7.0 6.5 6.0 5.5 5.0 4.5 4.0 3.5 3.0 2.5 2.0 1.5 1.0 0.5 0.0
f1 (ppm)
172.5
168.9
151.4
151.1
146.5
143.0
135.8
132.5
130.7
128.8
128.5
126.8
126.2
124.4
122.9
122.2
54.6
170 160 150 140 130 120 110 100 90 80 70 60 50 40 30 20 10 0
f1 (ppm)

## Compound 3c

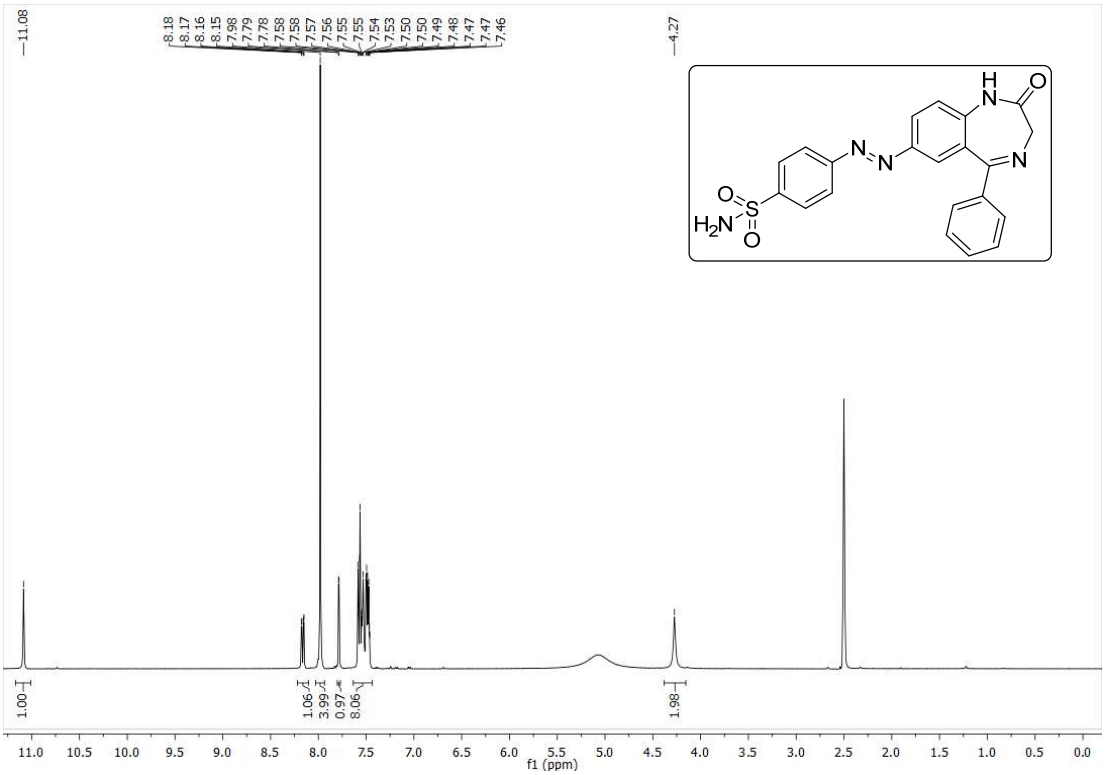
11.08
8.18
8.17
8.16
8.15
7.98
7.79
7.78
7.58
7.58
7.57
7.56
7.55
7.55
7.54
7.53
7.50
7.50
7.49
7.48
7.47
7.47
7.46
4.27
1.00
1.06
3.99
0.97
8.06
1.98
f1 (ppm)

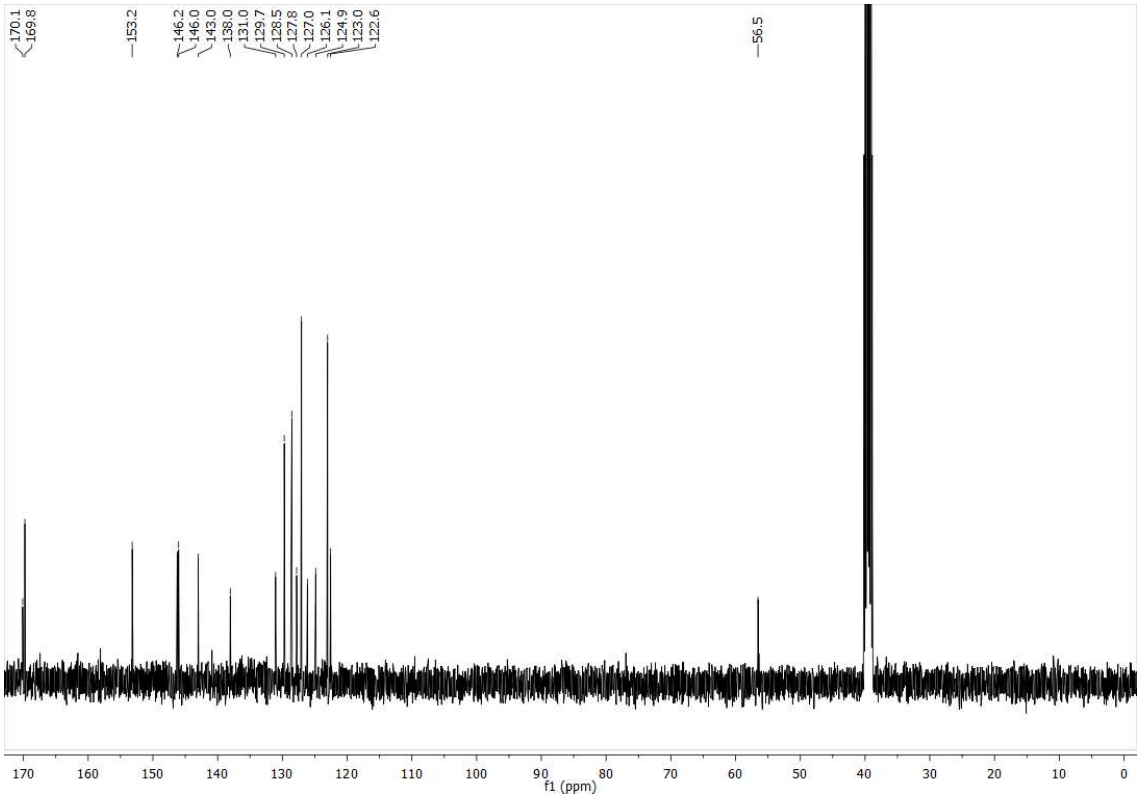
170.1
169.8
153.2
146.2
146.0
143.0
138.0
131.0
129.7
128.5
127.8
127.0
126.1
124.9
123.0
122.6
56.5
f1 (ppm)

## Compound 3d

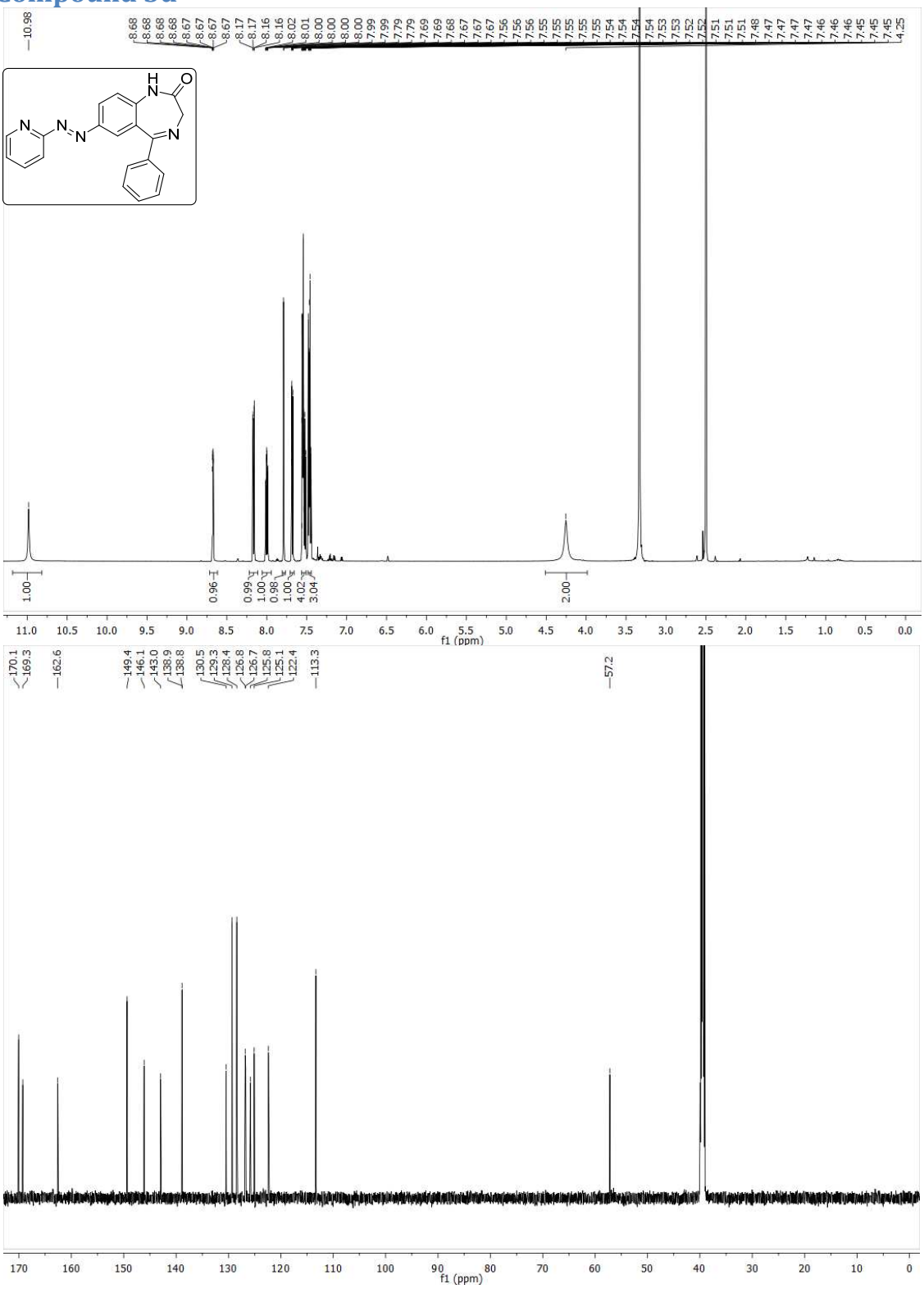
10.98
8.68
8.67
8.17
8.16
8.02
8.01
8.00
7.99
7.79
7.69
7.68
7.67
7.56
7.55
7.54
7.53
7.52
7.51
7.48
7.47
7.46
7.45
4.25
1.00
0.96
0.99
1.00
0.98
1.00
4.02
3.04
2.00
f1 (ppm)
170.1
169.3
162.6
149.4
146.1
143.0
138.9
138.8
130.5
129.3
128.4
126.8
126.7
125.8
125.1
122.4
113.3
57.2
f1 (ppm)